The impact of Sedimentary Coatings on the Diagenetic Nd Flux

April N. Abbott[1,2*], Brian A. Haley[1], James McManus[1,3]

[1]College of Earth, Ocean, and Atmospheric Sciences, Oregon State University, 104 CEOAS Admin. Bldg., Corvallis, OR 97331-5503

[2]now at Macquarie University, Department of Earth and Planetary Sciences, Sydney, NSW, 2109

[3]University of Akron, Department of Geoscience, Akron, OH 44325-4101

[*] Corresponding author, april.abbott@mq.edu.au

Abstract

Because ocean circulation impacts global heat transport, understanding the relationship between deep ocean circulation and climate is important for predicting the ocean's role in climate change. A common approach to reconstruct ocean circulation patterns employs the neodymium isotope compositions of authigenic phases recovered from marine sediments. In this approach, mild chemical extractions of these phases is thought to yield information regarding the ε_{Nd} of the bottom waters that are in contact with the underlying sediment package. However, recent pore fluid studies present evidence for neodymium cycling within the upper portions of the marine sediment package that drives a significant benthic flux of neodymium to the ocean. This internal sedimentary cycling has the potential to obfuscate any relationship between the neodymium signature recovered from the authigenic coating and the overlying neodymium signature of the seawater. For this manuscript, we present sedimentary leach results from three sites on the Oregon margin in the northeast Pacific Ocean. Our goal is to examine the potential

mechanisms controlling the exchange of Nd between the sedimentary package and the overlying water column, as well as the relationship between the ε_{Nd} composition of authigenic sedimentary coatings and that of the pore fluid. In our comparison of the neodymium concentrations and isotope compositions from the total sediment, sediment leachates, and pore fluid we find that the leachable components account for about half of the total solid-phase Nd, therefore representing a significant reservoir of reactive Nd within the sediment package. Based on these and other data, we propose that sediment diagenesis determines the ε_{Nd} of the pore fluid, which in turn controls the ε_{Nd} of the bottom water. Consistent with this notion, despite having 1 to 2 orders of magnitude greater Nd concentration than the bottom water, the pore fluid is still <0.001% of the total Nd reservoir in the upper sediment column. Therefore, the pore fluid reservoir is too small to maintain a unique signature, and instead must be controlled by the larger reservoir of Nd in the reactive coatings. In addition, to achieve mass balance, we find it necessary to invoke a cryptic radiogenic (ε_{Nd} of +10) trace mineral source of neodymium within the upper sediment column at our sites. When present, this cryptic trace metal results in more radiogenic pore fluid.

Keywords

Neodymium, diagenesis, benthic flux, ocean circulation

Highlights

- Sediment diagenesis determines pore fluid ε_{Nd}, which controls bottom water ε_{Nd}.
- Authigenic phases drive the diagenetic system, since they are a large, reactive Nd reservoir.

- Trace minerals can influence the pore fluid ε_{Nd}.

1.0 Introduction

The neodymium isotope composition (ε_{Nd}) of seawater is commonly used as a quasi-conservative tracer of ocean circulation (e.g. Frank 2002; Goldstein and Hemming, 2003). The neodymium isotope value is reported as ε_{Nd}, defined as $[(^{143}Nd_{sample}/^{144}Nd_{Sample})/(^{143}Nd_{CHUR}/^{144}Nd_{CHUR})\text{-}1] \times 10^4$ where CHUR is the Chondritic Uniform Reserve, used as an average earth value ($^{143}Nd/^{144}Nd$ =0.512638; Jacobsen and Wasserburg, 1980). The ε_{Nd} of bottom water is thought to be recorded in marine sedimentary authigenic phases, including Fe or Mn (oxy)hydroxides that are directly precipitated from seawater (Frank, 2002). The changes in the ε_{Nd} of these authigenic phases over time are therefore interpreted as shifts in global ocean circulation (e.g. Haley et al., 2008; Piotrowski et al., 2005; Rutberg et al., 2000). However, authigenic ferromanganese ε_{Nd} is likely influenced by processes during early sediment diagenesis (e.g. Elderfield et al., 1981; Elderfield and Sholkovitz, 1987; Grousset et al., 1988) and may represent a mix of *in situ* authigenic and preformed Fe-Mn oxyhydroxides (Bayon et al., 2004). Furthermore, remobilization of these Fe-Mn oxyhydroxides during early diagenesis may also bias the ferromanganese ε_{Nd} signature (e.g. Elderfield et al., 1981; Elderfield and Sholkovitz, 1987; Palmer and Elderfield, 1986). In addition to these diagenetic caveats, the interpretation of ε_{Nd} as a paleoproxy for circulation is dependent on the quasi-conservative behavior of Nd throughout the global ocean (Tachikawa et al., 2003) and the ability to consistently recover a bottom water ε_{Nd} signature from the sediment record. However, Nd is not conservative in the global oceans and its

behavior is not biogeochemically consistent with ε_{Nd} appearing to be conservative; a discrepancy coined the "Nd paradox" (Arsouze et al., 2009; Goldstein and Hemming, 2003; Jones et al., 2008).

The main source of Nd to the ocean has conventionally been assumed to be the riverine dissolved load with a minor contribution from atmospheric deposition (e.g. Elderfield et al., 1990; Jones et al., 1994). In addition to concerns that result from the Nd paradox, observed changes to water mass ε_{Nd} along margins imply the presence of an additional Nd source (e.g. Jeandel et al., 1998; 2007). Furthermore, models indicate that the current budget of Nd does not account for 95% of the ocean's Nd and cannot reproduce modern ε_{Nd} distributions without additional Nd sources (Arsouze et al., 2009; Jones et al., 2008). If the dissolved river flux supplies only a fraction of the ocean's Nd, then other Nd sources must control the global distribution of ε_{Nd}. The particulate Nd flux to the ocean is nearly 100 times that of the dissolved riverine Nd flux (Oelkers et al., 2011). Jeandel et al. (2015) propose that dissolution in the water column of less than 3% of this particulate load can account for the "missing" Nd in the ocean. Alternatively, we have proposed that the role of the particles is most significant within the sediments, through post depositional Nd release driven by sediment diagenesis (Abbott et al., 2015 a, b). This idea builds upon studies that have highlighted the importance of sediments as a source of Nd to the ocean (e.g. Abbott et al., 2015a, b; Arsouze et al., 2009; Bayon et al., 2011; Carter et al., 2012; Elderfield and Sholkovitz, 1987; Freslon et al., 2014; Grousset et al., 1988; Haley and Klinkhammer, 2003; Jeandel et al., 2007; Lacan and Jeandel 2001, 2005; Sholkovitz and Elderfield, 1988; Sholkovitz et al., 1989;

99 Tachikawa et al., 2003; Van de Flierdt et al., 2004; Wilson et al., 2013), and that this
100 benthic source likely determines the ε_{Nd} distribution of the deep ocean (Abbott et al.,
101 2015b).

102 The influence of the benthic flux on the bottom water ε_{Nd} will depend on both
103 the magnitude and the ε_{Nd} value of the flux (Abbott et al., 2015b). An understanding
104 of the mechanistic relationship among the sediment characteristics, the magnitude
105 of the flux, and the ε_{Nd} of the pore fluid is required to estimate the influence of the
106 benthic flux of Nd on bottom water ε_{Nd} along the ocean's flow path. Here, we attempt
107 to constrain the factors and processes that control the magnitude and ε_{Nd} signature
108 of the benthic flux.

109 **2.0 Methods**

110 Sediment cores were collected from three sites in the eastern North Pacific
111 (**Figure 1**) in October 2012 (HH1200 and HH3000) and July 2013 (HH200).
112 Detailed sample collection and core collection techniques are published elsewhere
113 (Abbott et al., 2015a; **Supplemental information**). These sites form an east-west
114 transect near the mouth of the Umpqua River on the Oregon margin in a region
115 influenced by seasonal upwelling. The sites are from water depths of 200 m
116 (HH200), 1200 m (HH1200), and 3000 m (HH3000). The oxygen minimum zone in
117 this region occurs between 500 and 1200 m water depth.

118 Sediment leaching procedures were used to collect an acid leachable fraction
119 and reducible fraction. Subsamples of the freeze-dried sediment were weighed (2-3
120 g dry weight) and transferred to acid-rinsed Falcon ® Blue Max 50 mL polystyrene
121 conical tubes. The leaching procedure began with three milli-Q water (MQ) rinses

each time shaken by hand for one minute and centrifuged for 15 minutes, and then decanted to remove salts. Next, a 20 mL buffered acetic acid leach solution (0.5 M sodium acetate and 3.5 M glacial acetic acid in MQ; pH 3.5-4) was added and shaken for 2 hours, centrifuged for 20 min, and 60% of the leachate was collected and stored in a clean Teflon vial (this solution will be referred to as the "acid leachable" fraction). The rationale for only collecting 60% of the leachate is that this approach reduces the risk of contamination from particles; the remaining 40% was discarded. Following the acetic acid and three more MQ rinses, a ~50 mM hydroxylamine leach solution (0.1M hydroxylamine hydrochloride, 5 M >99,9% pure glacial acetic acid and 0.7M sodium hydroxide in MQ; pH 3.5 - 4) was added and the solution was stirred for 2 hours, centrifuged for 20 min, and 60% of the leachate was collected and stored in clean Teflon (this solution will be referred to as the "reducible" fraction).

Leachate and total solid digest solutions were analyzed on the Thermo VG ExCell quadropole ICP-MS at the W.M. Keck Collaboratory for Plasma Mass Spectrometry at Oregon State University (ICP-MS specs in Abbott et al., 2015a) for rare earth element (REE) concentrations. REE concentrations for leachate and total solid are reported as ng REE per g dry sediment. Oxide formation on the ICP-MS was <3% based on monitoring of cerium oxide formation.

Total solid, leachate, and seawater samples were run through a series of columns to isolate the Sr and Nd fractions for isotope analyses. First, samples were eluted through columns consisting of 2 mL of AG-1x resin to remove Fe from the solution to increase the yield and efficiency of the remaining columns. The resin

145 was cleaned with 6 mL of 6M HNO_3, 6 mL MQ, and then conditioned with 6 mL of 6M
146 1x distilled HCl. Samples were then re-dissolved in 1 mL of 6M distilled HCl, and
147 centrifuged for 5 minutes at 13400 rpm before loading onto the column. Collection
148 of the sample began when the sample was loaded onto the column and completed
149 with 5 mL of 6M distilled HCl. The eluate was dried completely, redissolved in 1M
150 distilled HCl, and loaded onto cation exchange columns (1.8 mL AG50W-X8 HCl form
151 resin). The AG50W-X8 resin was loaded with MQ, cleaned with 6 mL of 6M distilled
152 HCl, and conditioned with 6 mL of 1M distilled HCl before the sample was loaded.
153 Samples were eluted with 3 mL of 1M distilled HCl, 6 mL of MQ, and 4 mL of 2M
154 distilled HNO_3 and then the Sr fraction was collected in 7 mL of 2M distilled HNO_3.
155 After the collection of the Sr fraction, the REE fraction was collected in 10 mL of 6M
156 distilled HNO_3.

157 The Sr fraction was further purified using 50 µL Sr Spec Resin (Eichrom®
158 part SR-B505, 50-100 µm). Resin was cleaned with 300 µL of H_2SO_4, MQ, and 3M
159 HNO_3 before the 50 µL sample was loaded in 3M HNO_3, and eluted with 600 µL of
160 3M HNO_3. Sr was then collected in 500 µL MQ. Immediately after collection, 3 mL of
161 3% HNO_3 was added to each sample. The samples were analyzed on the Nu Plasma
162 ICP-MS multi collector in the Keck Laboratory at Oregon State University. Precision
163 was determined by repeated analysis of an in-house standard, EMD, which yielded a
164 mean $^{87}Sr/^{86}Sr = 0.708185$ with a 2σ standard deviation of ±0.000051 (n=79).
165 National Bureau of Standards reference material 987 (NBS-987) was measured for
166 these analysis at $^{87}Sr/^{86}Sr = 0.710245$ with a 2σ standard deviation of ±0.000052 (n
167 = 91) normalized to $^{86}Sr/^{88}Sr = 0.1194$. NBS-987 and EMD were analyzed, at a

168 minimum, after every 6 samples and analyzed in replicate at the beginning and end
169 of every sample group.
170 Neodymium was isolated from the REE fraction using 2 mL of 50-100 μm
171 mesh Ln resin (Eichrom® part LN-B50-5). The column was cleaned with 4 mL of
172 6M HCl and 6 mL of MQ, and then conditioned in 4 mL of 0.1M HCl before the 0.5 mL
173 sample was loaded in 0.1M HCl. The column was eluted with 15 mL of 0.1M HCl and
174 0.25M HCl before Nd was collected in 8 mL of 0.25M HCl. The samples were
175 analyzed on the Nu Plasma multi-collector ICP-MS at Oregon State University for
176 ^{144}Nd and ^{143}Nd. The SpecPure standard was used for in-house reproducibility,
177 yielding a mean $^{143}Nd/^{144}Nd = 0.511205$ with a 2σ standard deviation of ±0.000014.
178 The JNdi-1 standard was used for normalization to $^{143}Nd/^{144}Nd = 0.512115$ with a
179 2σ standard deviation of ±0.000011 (reference value 0.512115 ± 0.000007 (Tanaka
180 et al., 2000)). JNdi-1 and SpecPure were analyzed, at minimum, after every 6
181 samples and analyzed in replicate at the beginning and end of every batch run. The
182 column chromatography procedural blank was ≤0.02 ppb Nd.

183 **3.0 Results**

184 **3.1 Pore Fluid**

185 Pore fluids are middle rare earth element (MREE) enriched relative to Post
186 Archaen Australian Shale (PAAS) at all three sites (**Figure 2**, Abbott et al., 2015a).
187 Pore fluids are heavy rare earth element (HREE) depleted relative to the total solid
188 at HH200 and HH1200 (**Figure 2**). HH3000 pore fluids can be either depleted or
189 enriched in HREE relative to the total solid depending on the interval, but they are
190 generally HREE enriched compared to HH200 and HH1200 pore fluids (**Figure 2**).

191 The maximum concentration of Nd in the pore fluid increases and occurs
192 deeper within the sediment column from HH200 to HH1200 to HH3000 (**Figure 3**,
193 Abbott et al 2015a, b). This trend does not correlate to any other measured variable
194 in the pore fluids (**Figure 3; Supplemental Information Table 2**). Specifically, the
195 maximum concentration of dissolved Fe in the pore fluid decreases in magnitude
196 and occurs deeper within the sediment column from HH200 (~80 μM, 6 cm) to
197 HH1200 (~35 μM, 9 cm) to HH3000 (~8 μM, 11 cm; **Figure 3**). Dissolved Mn is
198 below detection at HH200 and HH1200, but reaches concentrations of 50 μM at
199 HH3000. Additionally, the dissolved Li concentration profile at HH3000 has a
200 steeper decrease with depth than observed in the pore fluid Li concentration profile
201 at HH1200 (**Figure 3**). This decrease in dissolved Li is likely a result of Li
202 incorporation during authigenic clay mineral formation (e.g. Stoffyn-Egli and
203 Mackenzie, 1984). Li and P data are unavailable for pore fluids from HH200. At
204 HH1200 dissolved P increases downcore from ~4 μM in near surface pore fluids to
205 ~16 μM at 8 cm while dissolved P generally remains between 6 and 8 μM
206 throughout the measured pore fluids at HH3000 with the lowest (~6 μM) occurring
207 in the upper most pore fluids (**Figure 3)**. As an aside, if phosphate precipitation or
208 dissolution reactions were controlling REE concentrations (e.g. Schacht et al., 2010),
209 we might expect the concentrations of P to covary with the Nd in the pore fluids,
210 which is not the case. With the exception of the upper two data points from
211 HH1200, the ε_{Nd} of the pore fluids is relatively constant at each site (**Figure 3**) and
212 becomes less radiogenic from HH200 (average ε_{Nd} -0.2) to HH1200 (average ε_{Nd} -
213 1.5) to HH3000 (average ε_{Nd} -1.8; **Figure 3**; Abbott et al., 2015b). Deviations from

214 the site average pore fluid ε_{Nd} are largely restricted to the HH1200. We do not
215 attempt to account for these minor deviations in our model (discussed below) and
216 instead focus on the average pore fluid ε_{Nd} at each site, which represents first order
217 controls on the system. Pore fluid $^{87}Sr/^{86}Sr$ is indistinguishable from seawater at all
218 sites (**Figure 4**).

219 **3.2 Total Solid Phase**

220 Total solid phase characteristics show little variation among sites. Total solid
221 REE patterns are similar among all sites with both MREEs and HREEs enriched
222 relative to PAAS (**Figure 2**, Abbott et al., 2015a). At all sites, total solid ε_{Nd} ranges
223 between 0.0 and -2.5, but the average ε_{Nd} becomes less radiogenic from HH200 (-
224 1.4) to HH1200 (-1.8) to HH3000 (-2.2, **Figure 5**). The concentration of Nd in the
225 digests exhibits little variation within each core, but the concentration of Nd
226 increases slightly with increasing water depth from HH200 (average 14 $\mu g\ g^{-1}$) to
227 HH1200 (average 16 $\mu g\ g^{-1}$) to HH3000 (average 17 $\mu g\ g^{-1}$). Bulk sediment organic
228 carbon concentrations average between 1.7% and 2.0% at all sites, with a slight
229 downcore decrease at HH1200 (**Figure 5**). Sedimentary Fe concentration is lowest
230 at HH200 (<5%) and greatest at HH1200 (5 - 8%; **Supplemental Information**
231 **Table 3**). Solid phase Mn concentrations are constant at ~450 ppm down-core at
232 both HH200 and HH1200. However, Mn concentrations reach almost 3600 ppm in
233 the surface sediments at HH3000 before decreasing to ~680 ppm at 7 cm
234 (**Supplemental Information Table 3**). Solid-phase Ca concentrations decrease
235 from HH200 (1.6 ± 0.03%) to HH1200 (1.4 ± 0.15%) to HH3000 (1.0± 0.08%,
236 (**Supplemental Information Table 3**). The $^{87}Sr/^{86}Sr$ of the sediment digests is

constant with depth at each site and becomes increasingly more radiogenic with increasing water depth: the average $^{87}Sr/^{86}Sr$ at HH200 (0.70757) < HH1200 (0.70816) < HH3000 (0.70977) (**Figure 5**). This off-shore trend in sedimentary $^{87}Sr/^{86}Sr$ is consistent with published values for the Cascadia basin (Carpentier et al., 2014). Only the total solid at HH3000 has Sr isotopic values more radiogenic than seawater (**Figure 4, Figure 5**).

The mineralogy of the marine sediment was similar among all sites (**Supplemental Information Figure 1**). All samples consisted of quartz, albite, a white mica (illite or muscovite) and a chlorite mineral (clinochlore). The only difference between pre-leach and post-leach sediments that we could observe in the XRD analyses was the presence of crystalline halite in the pre-leach sediments, likely formed during sample freeze-drying.

Grain size distributions were consistent downcore at each site for both pre- and post-leach measurements (**Supplemental Information Table 1**). Pre-leach and post-leach distributions are largely bimodal. The primary peak is at ~85 μm at HH200 and ~180 μm in pre-leach samples at both HH1200 and HH3000. The secondary peak is between 450 μm and 500 μm in all pre-leached samples. The overall mean of the pre-leach distribution increases from HH3000 (120 μm) to HH1200 (185 μm) to HH200 (205 μm; **Figure 6**). The post-leach distributions are bimodal, with the smallest overall mean at HH3000 (~20 μm) and larger means at both HH200 (~110 μm) and HH1200 (~140 μm; **Figure 6**). The most prevalent grain size is the smallest at HH3000 (~5 μm) and increases at HH1200 (~15 μm) and HH200 (~20 μm).

3.3 Leachates

The acid leachable solution becomes less radiogenic from HH200 (ε_{Nd} -1.1) and HH1200 (ε_{Nd} -1.2) to HH3000 (ε_{Nd} -1.9, **Figure 6**). The Fe in this leachate is on average higher at HH200 (87-141 μg mL^{-1}) than at HH1200 (66-135 μg mL^{-1}) and is lowest at HH3000 (53-66 μg mL^{-1}, **Supplemental Information Table 4; Figure 7**).

The reducible leachate has an average ε_{Nd} value between -0.6 and -0.9 at all sites with a maximum ε_{Nd} of 0.0 and a minimum ε_{Nd} of -1.7 (**Figure 6**; **Supplemental Information Table 5**). The ε_{Nd} of this leachate is relatively constant downcore at HH200 ($\varepsilon_{Nd} \sim$ -0.6) but changes downcore at 1200 m and 3000 m. Specifically, the reducible leachate at HH1200 m is more radiogenic with depth (ε_{Nd} -1.2 at 1.2 cm; ε_{Nd} -0.1 at 9.8 cm) and the reducible leachate at HH3000 m is less radiogenic with depth (ε_{Nd} -0.3 at 1.2 cm; -1.7 at 9.8 cm; **Figure 7**). Unlike in the acid leachable solution, the minimum (1300 μg g^{-1}) and maximum values (4300 μg g^{-1}) of Fe in the reducible leachate both occur at HH3000 (**Supplemental Information Table 4; Figure 7**).

At all locations, the ε_{Nd} of both leachates is more radiogenic than the total (pre-leach) solid (**Figure 7**). However, the acid leachable solution is most similar to the total solid at HH3000. The pore fluid is more radiogenic than both leachates at HH200, but only more radiogenic than the acid leachable solution at HH3000 (**Figure 7**). Reactive Nd (i.e., the sum of the two leachates) accounted for 55 to 70% of the Nd in the total solid with an average concentration per site between 5.4 and 8.2 μg Nd g^{-1} sed (**Supplemental Information Table 6, Supplemental Information Figure 3**). Of the leachable Nd, 45% was acid leachable and 55% was

reducible (**Supplemental Information Table 7**). The concentration of Nd in both leachates increases with depth at all sites (**Supplemental Information Figure 2**). The leachate REE pattern is MREE enriched and HREE depleted (**Figure 2**), and the acid leachable solution is indistinguishable from the REE pattern of the reducible leachate. We should note here as a point of emphasis and clarification that although the acid leachable and reducible leachate distributions do vary from experiment to experiment, the ε_{Nd} of each leachate phase appears to be robust and consistent among experiments. This point suggests that the leaching procedure, although not necessarily quantitative, is targeting the same phase in each experiment.

4.0 Discussion

We have previously shown that there is a flux of Nd from sediment pore fluids into ocean bottom water and have suggested that this flux controls the bottom water ε_{Nd} value (Abbott et al., 2015 b). Here we present a diagenetic framework that outlines the important solid-phase processes that define the observed Nd behavior in marine pore fluids. This model separates the upper sediment column into two primary reservoirs, the pore fluid and the total solid (**Figure 8**). We consider there to be three main sub-components of the total solid that may interact with the pore fluids: particulate organic carbon (POC), lithogenic, and authigenic phases. POC does not appear to be an important reservoir because POC concentrations among all sites are similar and do not covary with any of the Nd pools (**Figure 5**). While the lithogenic component is often considered refractory, the surrounding fluid phase can be influenced by mineral dissolution and secondary precipitation processes (e.g. Jeandel and Oelkers, 2015; Rousseau et al., 2015; Tachikawa et al., 1999). Therefore,

306 our model focuses on the lithogenic and authigenic components of the total solid
307 (**Figure 8**). It is important to emphasize that although we have various
308 compositional information regarding the sedimentary solid phases, our authigenic
309 component is operationally defined by our sediment leachate results.

310 **4.1 Authigenic phases**

311 The authigenic component is divided into acid leachable and reducible
312 fractions that are defined by experimental leaching procedures. The idea that the
313 different leaching reagents target different solid phases is supported by the Fe, Mn,
314 and ε_{Nd} characteristics measured in the leachates (**Figure 7**). Specifically, compared
315 to the acid leachable fraction, the Fe to Mn ratios are higher in the reducible fraction
316 and the ε_{Nd} signatures are generally more radiogenic in the reducible fraction. The
317 exception is at HH200 where the ε_{Nd} signatures of the acid leachable and reducible
318 fractions are similar. The acid leachable ε_{Nd} more closely resembles the pore fluid at
319 all sites than does the reducible fraction, suggesting that either the reducible phase
320 contributes less Nd to the pore fluid or that the redox chemistry of the reducing
321 leach effectively targets a specific phase. The net result is that the ε_{Nd} signature of
322 the authigenic coatings does not resemble the overlying water column at any site.
323 Since the Nd isotopic signature of Fe-Mn oxyhydroxides is considered a first
324 indication of the source of the oxides (e.g. Bayon et al., 2011), we therefore suggest
325 the REEs in the authigenic coatings are most likely acquired during early diagenesis,
326 consistent with alteration of the authigenic phases during early diagenesis (Bayon et
327 al., 2004; Elderfield et al., 1981; Elderfield and Sholkovtiz 1987; Froelich et al., 1979;
328 Grousset et al., 1988; Palmer and Elderfield, 1986).

329 The grain size distribution of the sediments can indicate the relative
330 importance of authigenic phases in a given sample. For example, at HH3000 the
331 pre-leach grain size distribution appears similar to the grain size distributions at
332 HH1200 and HH200. Within this distribution, there is a wide size distribution and
333 larger than expected grain size at our most distal site, HH3000 (**Figure 6**).
334 However, the post-leach sediments show a narrower, well-defined distribution of
335 smaller grain size. This shift from pre-leach to post-leach distribution is smaller at
336 both HH1200 and HH200 (**Figure 6**). We consider the unexpectedly large grains in
337 the pre-leach grain size distributions, especially seen at HH3000, to be an artifact of
338 coagulation of grains due to surface coatings (**Figure 6**). We therefore suggest that
339 the difference between pre- and post-leach grain size distributions indicates the
340 presence of authigenic phases, which influence the measured "size" of the grains.
341 Under this assumption, the greatest influence of the authigenic phase should be at
342 HH3000 where the shift between the pre- and post-leach grain size distributions is
343 the greatest (**Figure 6**). Indeed, the largest change in grain size distribution
344 (HH3000) corresponds to the highest percent of leachable Nd at HH3000 (**Figure**
345 **6**). The greatest pore fluid concentrations of Nd at HH3000 are also concurrent with
346 the largest fraction of REEs recovered in the combined leachate (i.e., authigenic)
347 phases (**Figure 6**) indicating that the pore fluid Nd concentration is proportional to
348 the amount of authigenic phases in the sediment. In other words, we suggest that
349 diagenetic processes are controlling pore fluid Nd concentrations as well as pore
350 fluid ε_{Nd}.

In our model, the lithogenic component is allowed to release Nd to the pore fluids but does not acquire Nd from the pore fluids, while the authigenic phases are not only formed from pore water, but are able to exchange with the surrounding pore fluid (**Figure 8**). Thus, we expect the authigenic phases to have the same ε_{Nd} as the pore fluid. However, the observed leachates do not resemble the ε_{Nd} of the pore fluid (**Figure 6**). We therefore propose that the ε_{Nd} and Nd concentration of the operationally defined authigenic phases (leachates) likely represents a combination of "true" authigenic phases and lithogenic contamination. Specifically, the leachates are recovering Nd from lithogenic phases in addition to the authigenic phases in the sediment samples. We suggest this additional lithogenic input is not readily contributing to the pore fluid based on the difference in ε_{Nd} between the pore fluid and the leachates. We suggest that the pore fluid is a robust indicator of the 'true' authigenic phase ε_{Nd} because of the exchange between pore fluid and the authigenic phases, and we further suggest that any difference between the pore fluid and the leachate is an artifact of the leaching procedure targeting additional phases.

4.2 Constraints on pore fluid ε_{Nd}

Compared to the total solid phase, the Nd in the pore fluid accounts for less than 0.001% of the total Nd concentration per unit volume (**Figure 6; Supplemental Information Table 7**). Calculations of a sediment-pore fluid distribution coefficient (K_d) using background pore fluid Nd concentrations of 250 pmol L^{-1} measured at HH200 and total solid Nd concentrations of 13.8 μg g^{-1} result in a K_d of 1.8×10^5, similar to the minimum sediment-seawater K_d of 1.5×10^5 reported by Takata et al. (2016). Using seawater values from sites HH200 (12 pmol

374 L^{-1}) and HH3000 (36 pmol L^{-1}) our calculated sediment-seawater K_d ranges from 1.2
375 × 10^6 and 3.7 × 10^6, similar to the maximum sediment-seawater K_d of 1.8 ×10^6
376 reported by Takata et al. (2016). The small Nd concentration in the pore fluid
377 reservoir relative to the Nd concentration in the total solid phases means that pore
378 fluids cannot maintain a unique ε_{Nd} signature: even a small exchange between the
379 pore fluids and the authigenic or lithogenic reservoirs will dominate the pore fluid
380 signal. Being a surface exchange process, the exchange between pore fluid and the
381 authigenic phases is likely dependent upon the exposed surface area of the
382 authigenic phases, as has been observed with other surface processes (e.g.
383 dissolution, Schott et al., 2009, Schott et al., 2012). In this way, the greater the size
384 of the authigenic reservoir (i.e., the more authigenic coating is present), the greater
385 the capacity of the upper sediment column to sustain a benthic flux. Assuming
386 exchange between the authigenic phases and the pore fluid, the Nd release from the
387 authigenic phase must be greater than any Nd precipitation within an authigenic
388 phase for Nd to accumulate in the pore fluid. If this difference between release and
389 precipitation is a constant fraction of the authigenic reservoir, then the resulting
390 buildup of Nd in the pore fluids will be greater in sediments with more authigenic
391 phases, as observed here.
392 As described above, we expect the pore fluid ε_{Nd} to resemble the ε_{Nd} of the
393 source of Nd to the fluids; however, the measured pore fluid ε_{Nd} is more radiogenic
394 than the total solid ε_{Nd}, the reducible ε_{Nd}, and the acid leachable ε_{Nd} at HH200
395 (**Figure 6**). Therefore, to be consistent, our model requires a more radiogenic
396 source of ε_{Nd} to be able to explain the pore fluid ε_{Nd} at HH200. The initial bottom

water chemistry of pore fluids cannot provide this radiogenic source because the mass of Nd derived from bottom water is quantitatively insignificant and because the bottom water is less radiogenic than the pore fluids. Of the acid leachable, the reducible, and the lithogenic components, the lithogenic component is the only ε_{Nd} not directly measured (**Table 1**). However, we can calculate the ε_{Nd} and Nd concentration for the lithogenic component, to determine whether the lithogenic component is a radiogenic Nd source. We calculate the lithogenic component as

$$\varepsilon\ \mathrm{Nd}_{Lith} = \frac{((\varepsilon\ \mathrm{Nd}_{Total} \times [Nd]_{Total}) - (\varepsilon\ \mathrm{Nd}_{Auth} \times [Nd]_{Auth}))}{[Nd]_{Lith}} \quad (1)$$

where the *Total* is the measured total solid phase, *Auth* is a weighted sum of the acid leachable and reducible leachates, and *Lith* is the remaining lithogenic component. The result of this calculation is an ε_{NdLith} of -2 at HH200, -2.5 at HH1200, and -3.1 at HH3000 (**Table 1**), meaning that as a whole, the lithogenic component cannot provide a source of radiogenic Nd. However, we know that the lithogenic component consists of multiple major mineral phases (e.g., quartz, albite, a white mica, and clinochlore; **Supplemental Information Figure 1**). Therefore, preferential contribution from a single mineral phase within the lithogenic component is possible. Preferential contribution is consistent with laboratory leaching experiments in which the ε_{Nd} obtained was dependent on the fraction of the particles reacting with the leach solution (Wilson et al., 2012; Wilson et al., 2013).

4.3 Cryptic trace mineral

A radiogenic trace mineral may provide the "unmeasured" radiogenic source required to explain the pore fluid ε_{Nd} signature in the absence of any measurable highly radiogenic source. This trace mineral adds complexity, but serves as an example as increasing pore fluid data sets become available for a more comprehensive model. Currently, the proposal of a trace mineral preferentially dominating the particulate-fluid interaction is consistent with observations in the modern ocean and in the laboratory (e.g. Jeandel et al., 2015; Pearce et al., 2013; Rousseau et al., 2015; Wilson et al., 2012; Wilson et al., 2013). Evidence for this radiogenic trace mineral exists in bottom water from HH200. At HH200, we were able to measure the ε_{Nd} signatures of a filtered bottom water sample and an unfiltered bottom water sample. Being closest to the shore, HH200 is likely to be most influenced by a reactive trace mineral, considering the release of Nd from suspended particulate matter is rapid (3 ± 1 weeks, Rousseau et al., 2015) and the more distal, deeper sediments have more developed and recycled authigenic phases. The unfiltered bottom water sample represents a combination of the filtered bottom water and what is essentially an acid leach of the particles in the water due to sample acidification. We observe that the ε_{Nd} of the unfiltered bottom water (ε_{NdUBW} = +0.7) is more radiogenic than the ε_{Nd} of the filtered bottom water (ε_{NdBW} = -1.8; **Table 1**). Assuming that the acidification of the unfiltered bottom water only adds Nd from the reactive trace mineral, and limiting the contribution of Nd to 20% of the concentration of Nd in the filtered bottom water, we can calculate the ε_{Nd} of the trace mineral needed to produce the change in ε_{Nd} between the unfiltered and filtered bottom water as:

$$\varepsilon\ \mathrm{Nd}_{UBW} \times [Nd]_{UBW} = \varepsilon\ \mathrm{Nd}_{Trace} \times [Nd]_{Trace} + \varepsilon\ \mathrm{Nd}_{BW} \times [Nd]_{BW} \quad (2)$$

The result is a trace mineral with $\varepsilon_{NdTrace}$ = +10 to produce the observed shift in bottom water ε_{Nd} (equation 2). An ε_{Nd} of +10 is within the range of minerals coming from the Depleted Western Terranes in the region, including the Intermontane Belt, Coast Mountain Belt, Cascade Arc, and Vancouver Island (ε_{Nd} 0 to +11; Carpentier et al., 2014). More specifically, the Paleozoic mid-oceanic ridge basalts that comprise the Cache Creek terrane included in the Depleted Western Terranes, have ε_{Nd} between +7.7 and 10.2 (Smith and Lambert, 1995). The possibility of basaltic particles that could alter fluid ε_{Nd} and contribute REES to the solution has previously been experimentally investigated (Pearce et al., 2013). Therefore, inferring that a trace amount of this locally sourced reactive mineral with $\varepsilon_{NdTrace}$ = +10 is present in the sediments along the Oregon margin is at least possible.

In our model the trace mineral reacts readily, resulting in a significant contribution of radiogenic Nd to the pore fluid in less mature shallow sediments (i.e. HH200) where this trace mineral is extant. At HH200, we can estimate the percent Nd in the pore fluid coming from the trace mineral as:

$$\varepsilon\ \mathrm{Nd}_{PW} \times [Nd]_{PW} = (\varepsilon\ \mathrm{Nd}_{AL} \times [Nd]_{AL}) + (\varepsilon\ \mathrm{Nd}_{Trace} \times [Nd]_{Trace}) \quad (3)$$

wherein we assume the difference between the measured pore fluid ε_{Nd} (ε_{NdPW}) and the acid leachable ε_{Nd} (ε_{NdAL}) is completely due to the contribution of Nd

to the pore fluid from a trace mineral with $\varepsilon_{NdTrace}$ of +10. The result is that only 3% of the Nd in the pore fluid at HH200 needs to come from the trace mineral to explain the observed ε_{NdPW} (-0.2; equation 3, **Figure 6**). Following the logic that the trace mineral is more prevalent in the shallow sediments closer to a terrestrial source, it follows that the trace mineral should be detectable in one or more local rivers. However, many rivers with differing ε_{Nd} signatures (e.g. VanLaningham et al., 2008) contribute to the Oregon margin. Additionally, seasonal variability in the ε_{Nd} signature of rivers could make detection of the cryptic phase time dependent (e.g. Viers et al., 2008). Combined, these complexities mean that extensive spatial and temporal sampling in each river would be necessary to discern the trace mineral in the riverine system.

We speculate that the contribution of radiogenic Nd from this trace mineral becomes less significant as the amount of the trace mineral remaining in the total solid decreases with sediment maturity (**Figure 8**). REE patterns support a greater contribution from such a reactive trace mineral in the less mature (shallower) sediments at HH200. That is, the REE pattern of the pore fluid is most different from the REE pattern of the total solid at HH200 and most similar at HH3000 (**Figure 2**). The similarity of the REE patterns of pore fluids and total solid at HH3000 is consistent with the absence of a reactive trace mineral in these more mature sediments. In addition to REE patterns, a decrease in the reactive trace mineral is supported by more radiogenic total solid at HH200 compared to HH3000 (**Figure 5, Table 1**). Specifically, the average total solid ε_{Nd} (ε_{NdTS}) changes from -1.4 at HH200 to -1.8 at HH1200 to -2.2 at HH3000. Using the $\varepsilon_{NdTrace}$ = +10 calculated above, we

488 can determine the percent of Nd in the trace mineral component of the total solid
489 (TS) at HH200 that is not present at HH3000 if the only factor changing the total
490 solid ε_{Nd} is the loss of the trace mineral offshore. We determine $[Nd]_{Trace}$ as
491
492 $$\varepsilon\ \mathrm{Nd}_{TS3000}\times[Nd]_{TS3000} = (\varepsilon\ \mathrm{Nd}_{TS200}\times[Nd]_{TS200}) - (\varepsilon\ \mathrm{Nd}_{Trace}\times[Nd]_{trace})$$
493 (4)
494
495 where $[Nd]_{trace}$ and $[Nd]_{TS3000}$ are fractions between 0 and 1 and must sum to
496 $[Nd]_{TS200}$ ($[Nd]_{TS200}$ =1). The result is that $[Nd]_{trace}$ is 0.09; in other words 9% of the
497 Nd in the total solid at HH200 is coming from the reactive trace mineral
498 ($\varepsilon_{NdTrace}$=+10). This calculation demonstrates that the difference in the total solid
499 ε_{Nd} between HH200 and HH3000 can be explained by the decreasing presence of the
500 trace mineral, consistent with our model for explaining observed pore fluid ε_{Nd}
501 (equation 4, **Figure 8**).
502 Acknowledging that Sr has different geochemistry than Nd, the $^{87}Sr/^{86}Sr$
503 measured in the pore fluid, leachates, and total solid phase are consistent with our
504 diagenetic model for Nd. The pore fluid Sr reservoir is small compared to the solid
505 phases, accounting for ~1% of the concentration of Sr in the upper sediment column
506 per unit volume. The pore fluid $^{87}Sr/^{86}Sr$ is within error of seawater (**Figure 4)**.
507 The $^{87}Sr/^{86}Sr$ of both leachates is between the $^{87}Sr/^{86}Sr$ of the pore fluid and the
508 $^{87}Sr/^{86}Sr$ of the total solid at all sites. As with leachate ε_{Nd}, the greatest deviation in
509 leachate $^{87}Sr/^{86}Sr$ from pore fluid $^{87}Sr/^{86}Sr$ occurs at HH200 supporting our
510 assertion that the leachates are contaminated with the lithogenic phase (**Figure 4**).

511 On average, the Sr in the acid leachable solution is 45% of the Sr in the upper
512 sediment column by volume. The remaining 55% of Sr is split evenly between the
513 reducible leachate and the refractory phase with a molar Sr/Ca of between 0.003
514 and 0.008 in all leachates (**Supplemental Information Table 4**). For the total solid,
515 the increase in $^{87}Sr/^{86}Sr$ from HH200 (0.707565) to HH3000 (0.709773) is
516 consistent with the corresponding decrease in ε_{Nd} (**Figure 5**). Both the lower
517 $^{87}Sr/^{86}Sr$ and higher ε_{Nd} at HH200 support a greater contribution from the depleted
518 western terranes than at HH1200 or HH3000 (depleted western terranes 0.702000-
519 0.706000; e.g. DePaolo and Wasserbug, 1976; Carpentier et al., 2014).

520 **4.4 Applicability to ε_{Nd} distribution of the global ocean**

521 In the modern ocean, a first order relationship has been observed between
522 salinity and ε_{Nd} (VonBlanckenburg, 1999). The core of North Atlantic Deep Water
523 maintains an ε_{Nd} of -13.5 along its flow path, becoming more radiogenic towards the
524 south with the input of more radiogenic bottom water from Southern Ocean deep
525 water formation. However, in the North Pacific, there is a change in the deep-water
526 ε_{Nd} signal that occurs despite the absence of deep-water formation. Isotopic models
527 have been unable to explain this alteration when ε_{Nd} is treated as a conservative
528 tracer with riverine point sources (Arsouze et al., 2009; Jones et al., 2008). We
529 suggest that the ε_{Nd} of the deep Pacific is instead determined by the ε_{Nd} of the
530 benthic flux. As seen at all of our sites, the ε_{Nd} of the flux provides a source that is
531 more radiogenic than the bottom water. Therefore, as the bottom water continues
532 to be exposed to the flux along its flow path, the ε_{Nd} of the bottom water becomes
533 more radiogenic. Models confirm that the addition of a deep Pacific source of

534 radiogenic Nd can bring model outputs from the interior ocean to within one ε unit
535 of modern observations (Jones et al., 2008). In this way the benthic flux of Nd to the
536 ocean can explain the observed ε_{Nd} gradient in the North Pacific, as well as the non-
537 conservative behavior of Nd in the water column. This "benthic flux" hypothesis has
538 the potential to fundamentally change our understanding of REE cycling and the
539 biogeochemical cycle of ε_{Nd} in the ocean. This hypothesis needs to be further
540 evaluated in other ocean basins and in a variety of sediment compositions.
541 Furthermore, this model implies that the use of authigenic coatings as a proxy for
542 bottom water ε_{Nd} in the past, may not, strictly speaking, be viable.

543 **5.0 Conclusions**

544 Pore fluid and sediment samples from three sites along the Oregon margin
545 were collected and analyzed to evaluate the role of sediment diagenesis on pore
546 fluid Nd composition. At these sites, sediment diagenesis dictates the Nd
547 concentrations and ε_{Nd} in pore fluids. Because the flux of pore fluid Nd is a major
548 source of Nd to the oceans, these diagenetic processes also can control the ε_{Nd}
549 distribution of bottom water in regions with a large benthic flux. We find no simple
550 relationship between diagenetic Nd enrichment and bulk mineralogy or organic
551 carbon degradation. The Nd in the pore fluid is <0.001% of the total Nd reservoir in
552 the sediment column, and because of the small size of this reservoir, it is sensitive to
553 small imbalances in exchanges with the total solid phase. Within the total solid, the
554 authigenic phases are a large and reactive reservoir of Nd, constituting ~50% of the
555 Nd in the total solid. We propose that the magnitude of the benthic flux at each site
556 is a result of the development of reactive authigenic phases during sediment

557 diagenesis. The more mature sediments at HH3000 support the greatest pore fluid
558 Nd concentrations and benthic flux. The less mature sediments at HH200 support
559 lower pore fluid Nd concentrations and have pore fluid ε_{Nd} influenced by the
560 presence of trace minerals that are more radiogenic in their composition. This
561 model provides a foundation for identifying sediment characteristics that are likely
562 to result in a large benthic flux or result in a benthic flux with an ε_{Nd} influenced by
563 exchange with a variety of lithogenic phases.
564
565 ***Acknowledgements***
566 This work was funded through NSF grants OCE-1147407 to JM and BH. The
567 University of Akron also supported JM's contributions to this study. We would like
568 to thank editor Derek Vance and three anonymous reviewers for their valuable
569 feedback and suggestions. We are also thankful for the support of the captain and
570 crew of the R.V. *Oceanus* during multiple expeditions. We also appreciate many
571 other individuals for their assistance. Chris Moser, Jesse Muratli, Paul Walczak, Chris
572 Holm, Meghan Megowan, Annie Hartwell, Nathan Ross, Valerie Maule, and Renee
573 Renn for help during the field and/or laboratory portions of this research; Burke
574 Hales for helpful conversations, GeomaticsResearch for aid in software development
575 for data processing; Andy Ungerer for ICP-MS facility support at Oregon State
576 University's W.M. Keck Collaboratory for Plasma Spectrometry; John Dilles and Carli
577 Duda for performing XRD analysis; and Chris Romsos and Chris Goldfinger for
578 assistance with grain size analysis.
579

References

Abbott, A.N., Haley, B., McManus, J., and Reimers, C. (2015a) The sedimentary source of dissolved rare earth elements to the ocean, *Geochimica et Cosmochimica Acta*, **154**, 186-200. doi: 10.1016/j.gca.2015.01.010

Abbott, A.N., Haley, B., and McManus, J. (2015b) Bottoms up: Sedimentary control of the deep North Pacific Ocean's εNd signature. *Geology*, **43**, 1035-1038. doi: 10.1130/G37114.1

Arsouze, T., Dutay, J.C., Lacan, F., Jeandel, C. (2009). Reconstructing the Nd oceanic cycle using a coupled dynamical—biogeochemical model. *Biogeosciences,* **6**, 2829-2846.

Bayon, G., German, C.R., Burton, K.W., Nesbitt, R.W., and Rogers, N. (2004). Sedimentary Fe-Mn oxyhydroxides as paleoceanographic archives and the role of aeolian flux in regulation oceanic dissolved REE. *Earth and Planetary Science Letters,* **224**, 477-492. Doi: 10.1016/j.epsl.2004.05.033

Bayon, G., Birot, D., Ruffine, L., Caprais, J.-C., Ponzevera, E., Bollinger, C., Donval, J.-P., Charlou, J.-L., Voisset, M., and Grimaud, S. (2011). Evidence for intense REE scavenging at cold seeps from the Niger Delta margin. *Earth and Planetary Science Letters*, **312**, 443-452. Doi: 10.1016/j.epsl.2011.10.008

Carpentier, M., Weis, D., and Chauvel, C., 2014. Fractionation of Sr and Hf isotopes by mineral sorting in Cascadia Basin terrigenous sediments. *Chemical Geology*, **382**, 67-82. http://dx.doi.org/10.1016/j.chemgeo.2014.05.028

Carter, P., Vance, D., Hillenbrand, C.D., Smith, J.A., and Shoosmith, D.R. (2012) The neodymium isotopic composition of waters masses in the eastern Pacific sector of the Southern Ocean. *Geochimica et Cosmochimica Acta*, **79**, 41-79. doi: 10.1016/j.gca.2011.11.034

DePaolo, D.J., and Wasserburg, G.J. (1976). Inferences about magma sources and mantle structure from variations of $^{143}Nd/^{144}Nd$. *Geophysical Research Letters*, **3**, 743-746.

Elderfield, H., Hawkesworth, C.J., and Greaves, M.J. (1981) Rare earth element geochemistry of oceanic ferromanganese nodules and associated sediments. *Geochimica et Cosmochimica Acta*, **45**, 513-528.

Elderfield, H., and Sholkovitz, E.R. (1987). Rare earth elements in the pore waters of reducing nearshore sediments. *Earth and Planetary Science Letters*, **82**, 280-288.

Elderfield, H., Upstill-Goddard, R., and Sholkovitz, E.R. (1990). The rare earth elements in rivers, estuaries, and coastal seas and their significance to the composition of ocean waters. *Geochimica et Cosmochimica Acta*, **54,** 971-991.

Frank, M. (2002). Radiogenic Isotopes: Tracers of Past Ocean Circulation and Erosional Input. *Reviews of Geophysics,* **40***.* doi:10.1029/2000RG000094.

Freslon, N., Bayon, G., Toucanne, S., Bermell, S., Bollinger, C., Chéron, S., Etoubleau, J., Germain, Y, Khripounoff, A., Ponzevera, E., and Rouget, M.-L. (2014) Rare earth elements and neodymium isotopes in sedimentary organic matter. *Geochimica et Cosmochimica Acta*, **140**, 177-198. doi: 10.1016/j.gca.2014.05.016

625 Goldstein, S.L., Hemming, S.R. (2003). Long lived isotopic tracers in oceanography,
626 paleoceanography, and ice sheet dynamics. In: Elderfield, H. (Ed.), Treatise on
627 Geochemistry. Elsevier Pergamon press, Amsterdam. Chpt 6.17.
628 Grousset, F.E., Biscaye, P.E., Zindler, A., Prospero, J., and Chester, R. (1988).
629 Neodymium isotopes as tracers in marine sediments and aerosols: North
630 Atlantic. *Earth and Planetary Science Letters*, **87**, 367-378.
631 Haley, B., and Klinkhammer, G. (2003). Complete separation of rare earth elements
632 from small volume seawater samples by automated ion chromatography:
633 method development and application to benthic flux. *Marine Chemistry,* **82**,
634 197-220. Doi: 10.1016/SO304-4203(03)00070-7
635 Haley, B.A., Klinkhammer, G.P., McManus, J. (2004) Rare earth elements in pore
636 waters of marine sediments. *Geochimica et Cosmochimica Acta*, **68**, 1265-
637 1279. Doi:10.1016/j.gca.2003.09.012
638 Haley, B.A., Frank, M., Spielhagen, R.F., Eisenhauer, A. (2008) Influence of brine
639 formation on Arctic Ocean circulation over the past 15 million years. *Nature*
640 *Geoscience,* **1,** 68-72.
641 Henderson, G.M., Martel, D.J., Onions, R.K., and Shackleton, N.J. (1994). Evolution of
642 seawater Sr-87/Sr-86 over the last 400 ka – the absence of glacial-interglacial
643 cycles. *Earth and Planetary Science Letters*, **128**, 643-651.
644 Jacobsen, S.B., Wasserburg, G.J. (1980). Sm-Nd isotopic composition of chondrites.
645 *Earth and Planetary Science Letters,* **50**, 139-155.
646 Jeandel, C., Thouron, D., and Fieux, M. (1998) Concentrations and isotopic
647 compositions of neodymium in the eastern Indian Ocean and Indonesian
648 straits. *Geochimica et Cosmochimica Acta*, **62**, 2597-2607.
649 Jeandel, C., Arsouze, T., Lacan, F., Techine, P., Dutay, J.C. (2007). Isotopic Nd
650 compositions and concentrations of the lithogenic inputs into the ocean: a
651 compilation, with an emphasis on the margins. *Chemical Geology,* **239**, 156-
652 164.
653 Jeandel, C., and Oelkers, E.H. (2015). The influence of terrigenous particulate
654 material dissolution on ocean chemistry and global element cycles. *Chemical*
655 *Geology*, **395**, 50-66. doi 10.1016/j.chemgeo.2014.12.001
656 Jones, C.E., Halliday, A.N., Rea, D.K., and Owen, R.M. (1994). Neodymium isotopic
657 variations in North Pacific modern silicate sediment and the insignificance of
658 detrital REE contributions to seawater. *Earth and Planetary Science Letters*,
659 **127**, 55-66.
660 Jones, K.M., Khatiwala, S.P., Goldstein, S.L., Hemming, S.R., and van de Flierdt, T.
661 (2008). Modeling the distribution of Nd isotopes in the oceans using an ocean
662 general circulation model. *Earth and Planetary Science Letters*, **272**, 610-619,
663 doi: 10.1016/j.epsl.2008.05.027
664 Lacan, F., and Jeandel, C. (2001). Tracing Papua New Guinea imprint on the central
665 Equatorial Pacific Ocean using neodymium isotopic compositions and rare
666 earth element patterns. *Earth and Planetary Science Letters,* **186**, 497-512.
667 Lacan, F., and Jeandel, C. (2005). Acquistion of the neodymium isotopic
668 composition of the North Atlantic Deep Water. *Geochemistry, Geophysics,*
669 *Geosystems, 6, Q12008.* doi:10.1029/2005GC00956.

Oelkers, E.H., Gislason, S.R., Eiriksdottir, E.S., Jones, M., Pearce, C.R., and Jeandel, C. (2011). *Applied Geochemistry*, **26**, 365-369. doi: 10.1016/j.apgeochem.2011.03.062

Palmer, M.R., and Elderfield, H. (1986) Rare earth elements and neodymium isotopes in ferromanganese oxide coatings of Cenozoic foraminifera from the Atlantic Ocean. *Geochimica et Cosmochimica Acta*, **50**, 409-417.

Pearce, C.R., Jones, M.T., Oelkers, E.H., Pradoux, C., and Jeandel, C. (2013) The effect of particulate dissolution on the neodymium (Nd) isotope and Rare Earth Element (REE) composition of seawater. *Earth and Planetary Science Letters*, **369-370**, 138-147. Doi: 10.1016/j.epsl.2013.03.023

Piotrowski, A.M., Goldstein, S.L., Hemming, S.H., Fairbanks, R.G. (2005) Temporal relationships of carbon cycling and ocean circulation at glacial boundaries. *Science,* **307**, 1933–1938. doi:10.1126/science.1104883.

Rousseau, T.C.C., Sonke, J.E., Chmeleff, J., van Beek, P., Souhaut, M., Boaventura, G., Syler, P., and C. Jeandel (2015). Rapid neodymium release to marine waters from lithogenic sediments in the Amazon estuary. *Nature Communications,* doi: 10.1038/ncomms8592

Rutberg, R.L., Hemming, S.H., Goldstein, S.L. (2000) Reduced North Atlantic Deep Water flux to the glacial Southern Ocean inferred from neodymium isotope ratios. *Nature,* **405**, 935– 938.

Schacht, U., Wallmann, K., and Kutterolf, S. (2010) The influence of volcanic ash alteration on the REE composition of marine pore waters. *Journal of Geochemical Exploration*, **106**, 176-187. Doi: 10.1016/j.gexplo.2010.02.006

Schott, J., Pokrovsky, O.S., and Oelkers, E.H. (2009). The link between mineral dissolution/precipitation kinestics and solution chemistry. *Reviews in Mineralogy & Geochemistry,* **70**, 207-258. doi: 10.2138/rmg.2009.70.6

Schott, J., Oelkers, E.H., Bénzéth, P., Goddéris, Y., and François, L. (2012). Can accurate kinetic laws be created to describe chemical weathering? *Comptes Rendus Geoscience*, **344**, 568-585. doi:10.1016/j.crte.2012.10.005

Sholkovitz, E.R., and Elderfield, H. (1988). Cycling of dissolved rare earth elements in Chesapeake Bay. *Global Biogeochemical Cycles*, **2**, 157-176.

Sholkovitz, E.R., Piepgras, D.J., and Jacobsen, S.B. (1989). The pore water chemistry of rare earth elements in Buzzards Bay sediments. *Geochimica et Cosmochimica Acta*, **53**, 2847-1856.

Smith, A.D., and Lambert, R.StJ. (1995) Nd, Sr, and Pb isotopic evidence for contrasting origins of late Paleozoic volcanic rocks from the Slide Mountain and Cache Creek terranes, south-central British Columbia. *Candian Journal of Earth Sciences,* **32,** 447-459.

Stoffyn-Egli, P., and Mackenzie, F.T. (1984) Mass balance of dissolved lithium in the oceans. *Geochimica et Cosmochimica Acta*, **48**, 859-872.

Tachikawa K., Jeandel C. and Roy-Barman M. (1999) A new approach to the Nd residence time in the ocean: the role of atmospheric inputs. *Earth and Planetary Science Letters*, **170**, 433-446.

Tachikawa, K., Athias, V., Jeandel, C. (2003). Neodymium budget in the ocean and paleoceanographic implications. *Journal of Geophysical Research*, **108**, 3254. Doi:10.1029/1999JC000285.

716 Takata, H., Aono, T., Tagami, K., Uchida, S. (2016). A new approach to evaluate
717 factors controlling elemental sediment-seawater distribution coefficients (K_d)
718 in coastal regions, Japan. *Science of the Total Environment*, **543**, 315-325. doi:
719 10.1016/j.scitotenv.2015.11.034
720 Tanaka, T., Togashi, S., Kamioka, H., Amakawa, H., Kagami, H., Hamamoto, T.,
721 Yuhara, M., Orihashi, Y., Yoneda, S., Shimizu, H., Kunimaru, T., Takahashi, K.,
722 Yanagi, T., Nakano, T., Fujimaki, H., Shinjo, R., Asahara, Y., Tanimizu, M. and
723 Dragusanu, C. (2000) JNdi-1: a neodymium isotopic reference in consistency
724 with LaJolla neodymium. *Chemical Geology,* **168**, 279–281.
725 van de Flierdt, T., Frank, M., Lee, D.-C., Halliday, A.N., Reynolds, B.C., and Hein, J.R.
726 (2004) New constraints on the sources and behavior of neodymium and
727 hafnium in seawater from Pacific Ocean ferromanganese crusts. *Geochimica*
728 *et Cosmochimica Acta*, **68**, 3827-3843.
729 Von Blanckenburg (1999). Tracing Past Ocean Circulation? *Science*, **286**, 1862-
730 1863. doi: 10.1126/science.286.5446.1862a
731 Wilson, D.J., Piotrowski, A.M., Galy, A., and McCave, I.N. (2012) A boundary
732 exchange influence on deglacial neodymium isotope records from the deep
733 western Indian Ocean. *Earth and Planetary Science Letters*, **341-344**, 35-47.
734 doi: 10.1016/j.epsl.2012.06.009
735 Wilson, D.J., Piotrowski, A.M., Galy, A., and Clegg, J.A. (2013). Reactivity of
736 neodymium carriers in deep sea sediments: Implications for boundary
737 exchange and paleoceanography. *Geochimica et Cosmochimica Acta*, **109**, 197-
738 221.

Main Text Figure and Table Captions

Figure 1 *Study Sites.* Map shows the location of study sites at water depths of 200 m, 500 m, 1200 m, and 3000 m on the Oregon Margin in the northeast Pacific Ocean. The benthic flux of Nd to the ocean was calculated at 200 m, 1200 m, and 3000 m (Abbott et al., 2015a,b). Water column profiles show dissolved oxygen (left) and ε_{Nd} (right). The dissolved oxygen profile is only shown at 3000 m, as the profiles were indistinguishable among sites at this scale. ε_{Nd} is shown for HH200 (squares), HH1200 (diamonds), and HH3000 (circles).

Figure 2 *Rare Earth Element Patterns.* REEs are normalized to PAAS and Pr. Pr normalization is based on published pore fluid Pr values from these sites (Abbott et al., 2015a). The Pr normalization allows direct comparison of the pattern variability in the lower absolute concentration samples to the patterns in the higher concentration samples. Total solid (black) and total leachate (striped) represents the range in pattern from all sites. Pore fluid patterns are shown individually for HH200 (pink), HH1200 (blue), and HH3000 (green). The reader is referred to the web version of this article for interpretation of the color version of this figure.

Figure 3 *Fluid Phase Characteristics.* Pore fluid profiles from **A)** HH200, **B)** HH1200, and **C)** HH3000 for dissolved iron, manganese, lithium, phosphorous, neodymium and ε_{Nd}. Mn was below the detection limit at HH200 and HH1200 for all sampled intervals. Li and P data are not available from HH200. Error bars for Fe, Mn, P, and Nd are smaller than symbol size. Black arrows on ε_{Nd} profiles indicate bottom water ε_{Nd} signatures.

Figure 4 *$^{87}Sr/^{86}Sr$.* $^{87}Sr/^{86}Sr$ for acid leachable (triangle) and reducible leachates (diamonds), total solid (solid squares), and pore fluids (striped squares). Pore fluid $^{87}Sr/^{86}Sr$ is indistinguishable from seawater (grey shading, 0.70918, Henderson et al., 2004) at all sites. Error bars represent 2σ. a) Expanded y scale to display acid leachable variations and b) full y scale to display variations in all phases.

Figure 5 *Solid Phase Characteristics.* Total solid profiles from **A)** HH200, **B)** HH1200, and **C)** HH3000 for ε_{Nd}, Nd concentration, percent organic carbon (%OC), Fe/Al, Mn/Al, and $^{87}Sr/^{86}Sr$. The shaded bar for $^{87}Sr/^{86}Sr$ indicates the global seawater value. Parentheses indicate values not included in interpretations.

Figure 6 *Mechanism Indicators*. **A)** ε_{Nd} profiles for the acid leachable (light grey), the reducible (dark grey) fractions, the total solid (black), and the pore fluid (striped) for HH200, HH1200, and HH3000. **B)** Relative distribution of Nd among acid leachable (light grey), reducible(dark grey), refractory phase (black), and pore fluid (values) per cubic centimeter for HH200, HH1200, and HH3000. **C)** Average grain size distributions for pre-leach (black outline) and post-leach (grey shading) samples from HH200, HH1200, and HH3000.

Figure 7 *Leachate Characteristics.* Fe, Mn, Fe/Mn, Fe/Al, Mn/Al and ε_{Nd} for **A)** acid leachable and **B)** reducible fractions from HH200 (squares), HH1200 (triangles), and HH3000 (circles).

Figure 8 *Diagenetic Model.* Schematic representation of the sources and sinks of Nd to the pore fluids at a shallow, less evolved site such as HH200 **(A)** and a deeper, more diagenetically evolved site such as HH3000 **(B)**. Total solid phase includes a trace mineral phase (black dots), an authigenic labile coating, authigenic oxides and a lithogenic (refractory) component. The particle is drawn approximately to scale. Calculated ε_{Nd} values are in *italics*, measured ε_{Nd} values are in **bold**. All concentrations are in ng cm^{-3}.

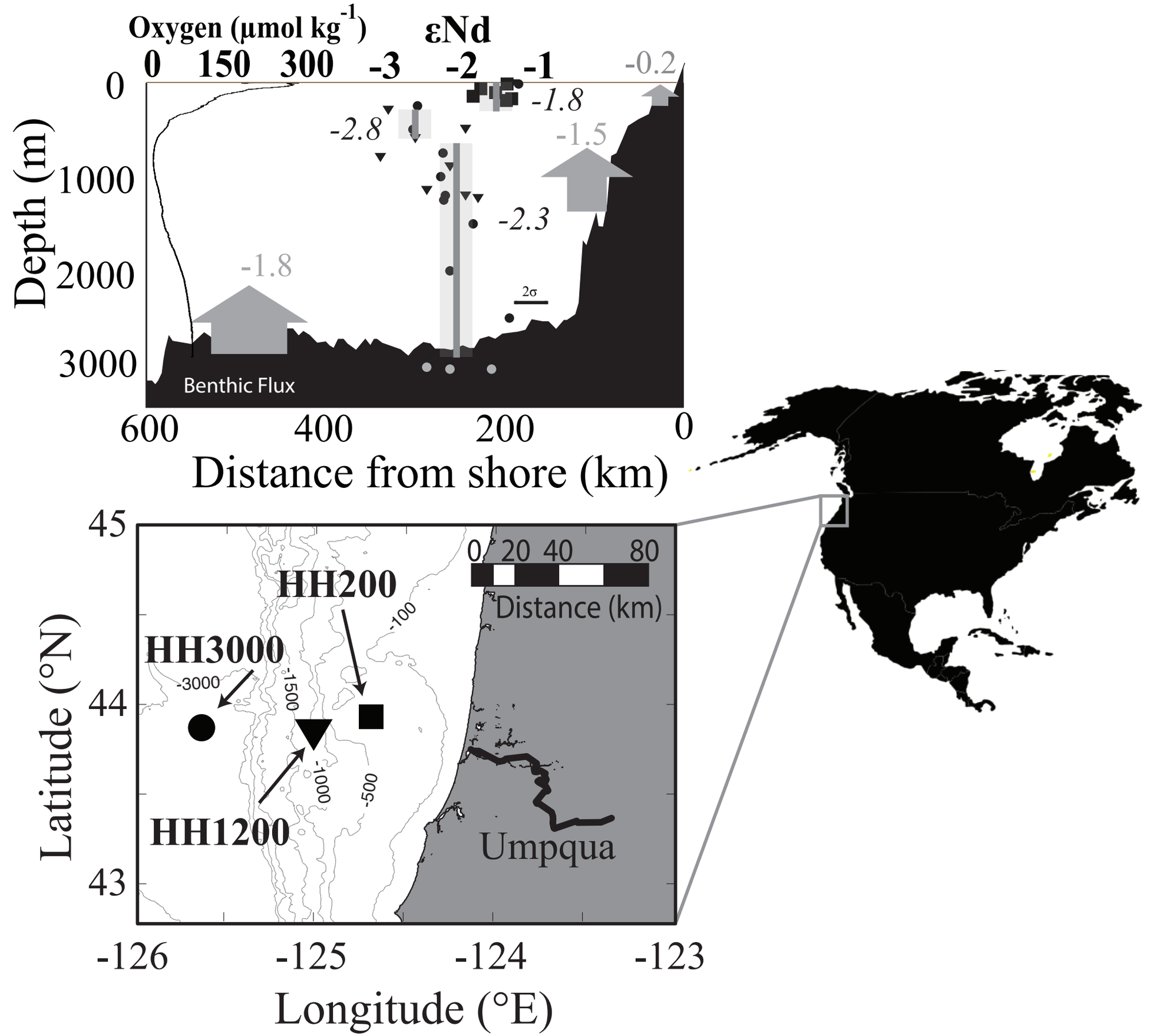
Oxygen (µmol kg-1)
εNd
0 150 300
-3 -2 -1
0
1000
2000
3000
Depth (m)
-0.2
-1.8
-2.8
-1.5
-2.3
-1.8
2σ
Benthic Flux
600 400 200 0
Distance from shore (km)
45
44
43
Latitude (°N)
0 20 40 80
Distance (km)
HH200
HH3000
HH1200
-100
-3000
-1500
-1000
-500
Umpqua
-126 -125 -124 -123
Longitude (°E)

Figure 2

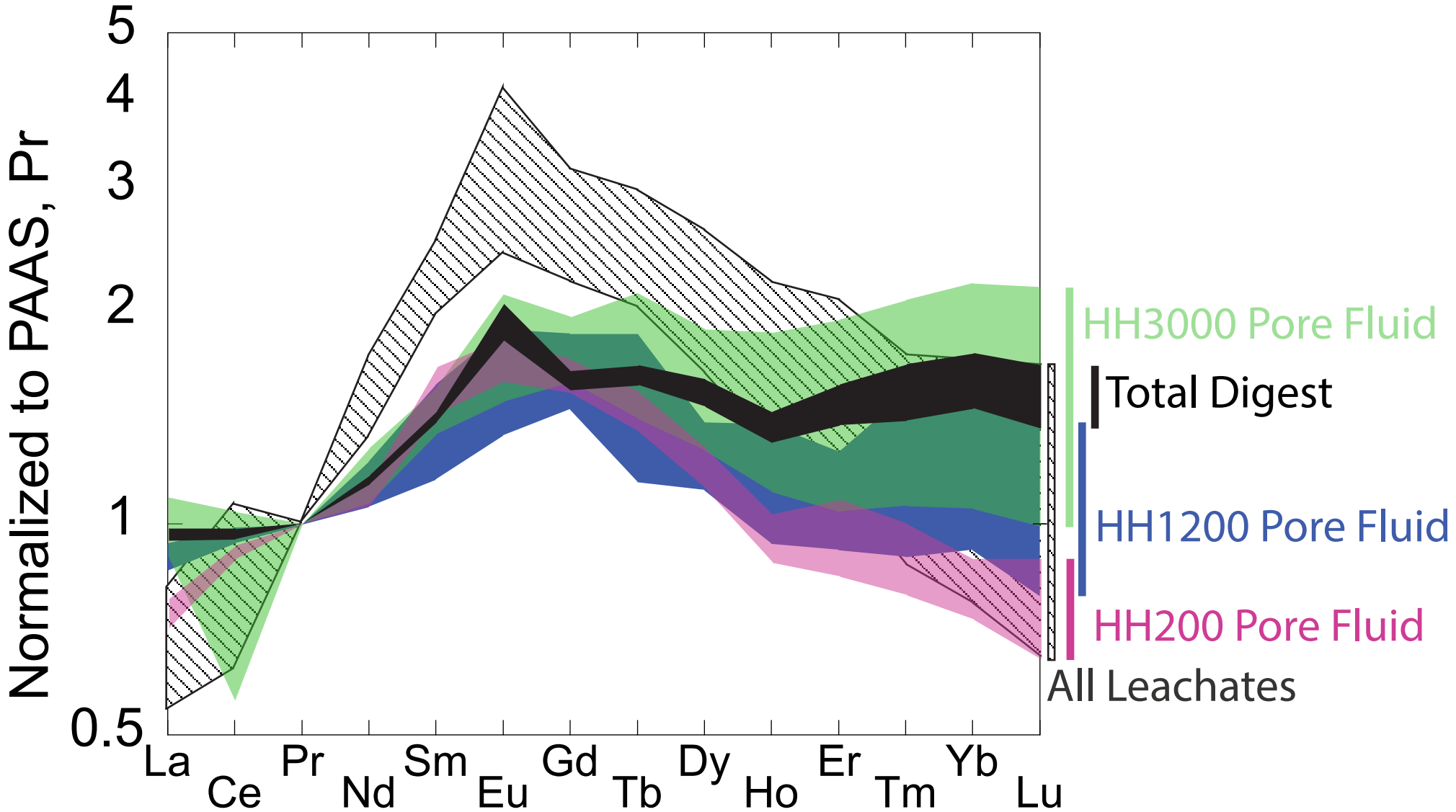
Normalized to PAAS, Pr
5
4
3
2
1
0.5
La
Ce
Pr
Nd
Sm
Eu
Gd
Tb
Dy
Ho
Er
Tm
Yb
Lu
HH3000 Pore Fluid
Total Digest
HH1200 Pore Fluid
HH200 Pore Fluid
All Leachates

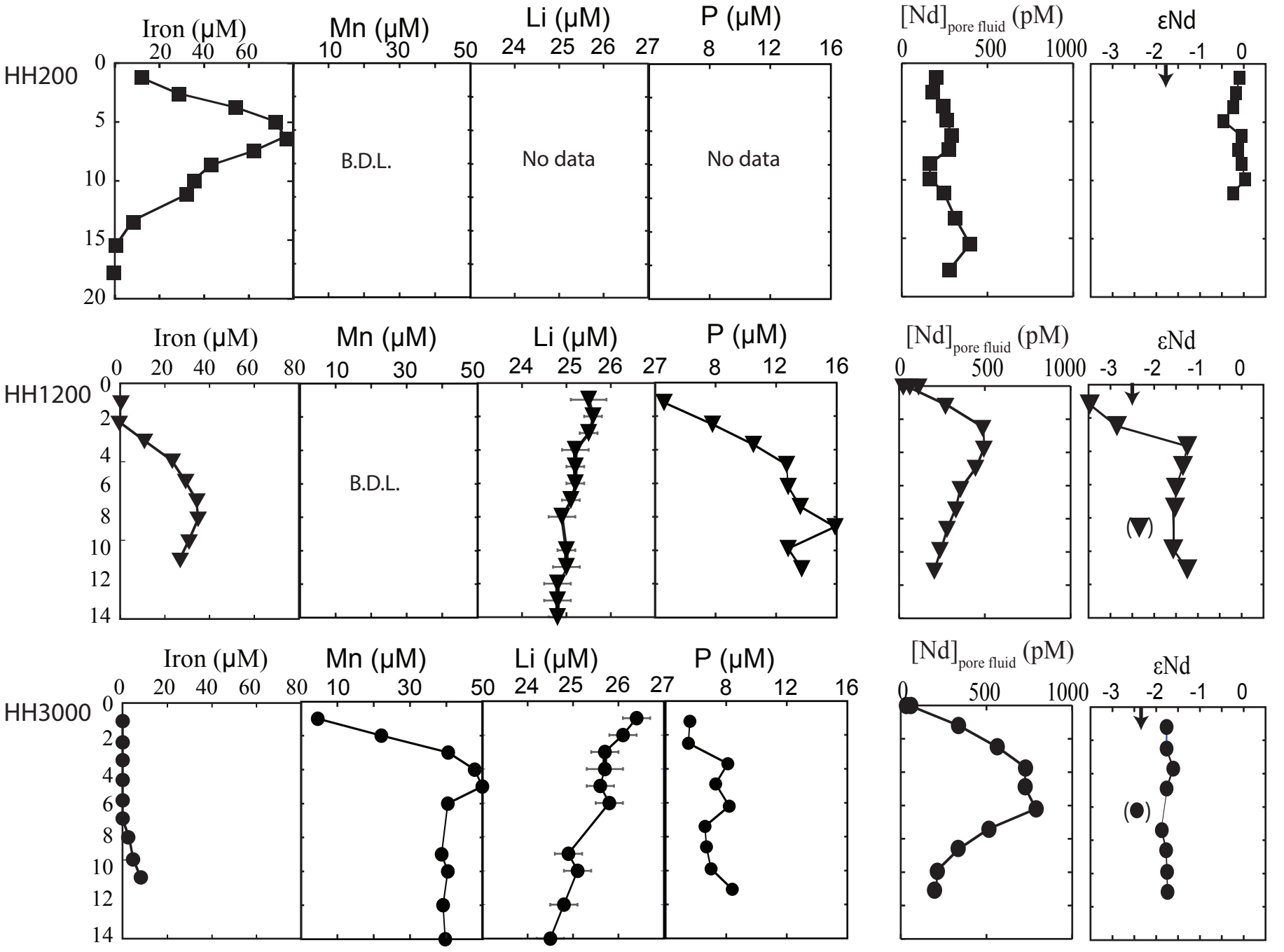
HH200
Iron (μM)
Mn (μM)
Li (μM)
P (μM)
B.D.L.
No data
No data
[Nd]pore fluid (pM)
εNd
HH1200
Iron (μM)
Mn (μM)
Li (μM)
P (μM)
B.D.L.
[Nd]pore fluid (pM)
εNd
HH3000
Iron (μM)
Mn (μM)
Li (μM)
P (μM)
[Nd]pore fluid (pM)
εNd

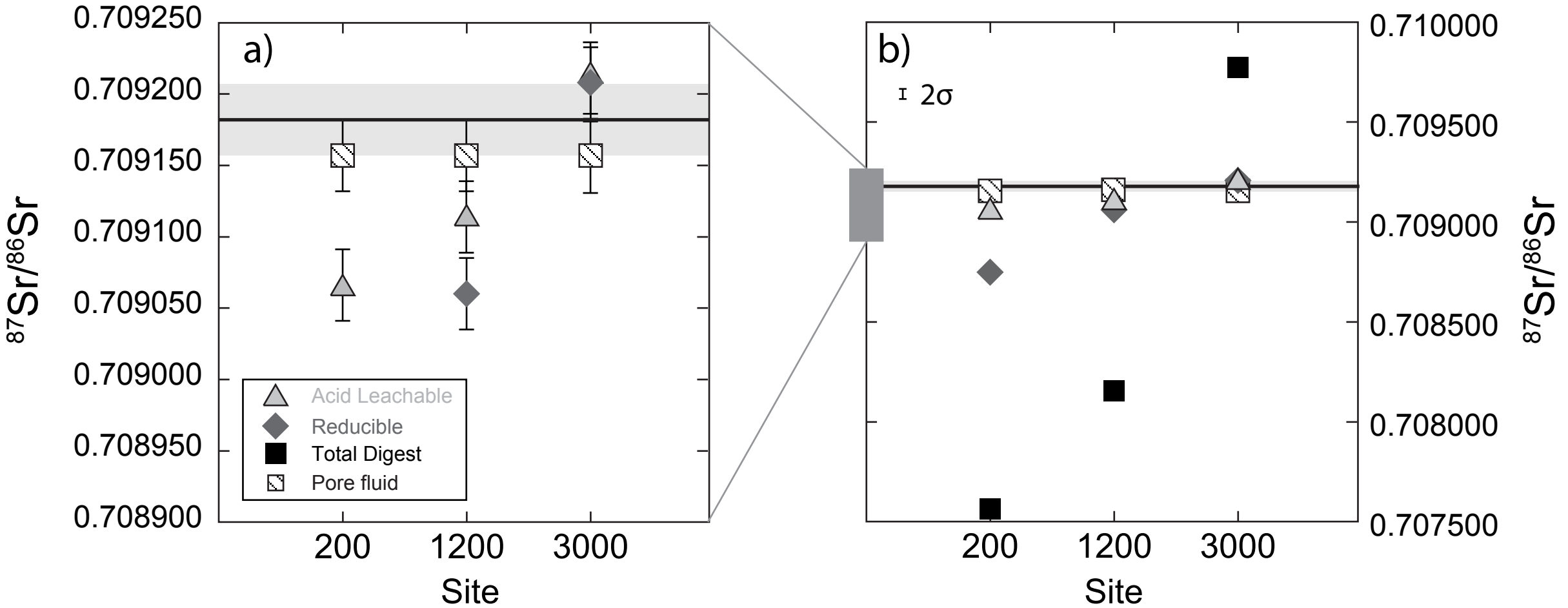
a)
b)
2σ
Acid Leachable
Reducible
Total Digest
Pore fluid
$^{87}Sr/^{86}Sr$
Site
0.709250
0.709200
0.709150
0.709100
0.709050
0.709000
0.708950
0.708900
0.710000
0.709500
0.709000
0.708500
0.708000
0.707500
200
1200
3000

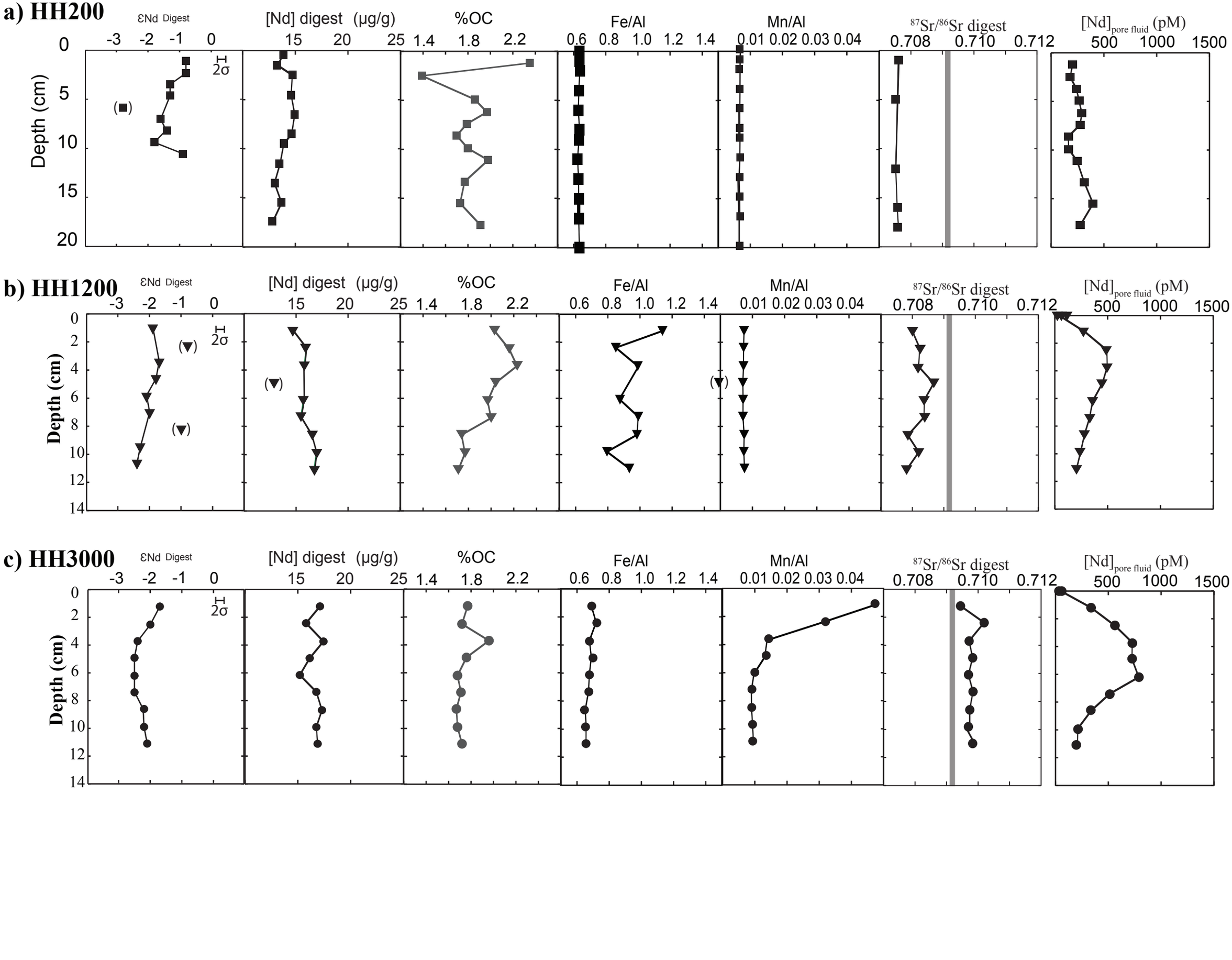
a) HH200
εNd Digest
[Nd] digest (μg/g)
%OC
Fe/Al
Mn/Al
87Sr/86Sr digest
[Nd]pore fluid (pM)
Depth (cm)
2σ
b) HH1200
c) HH3000

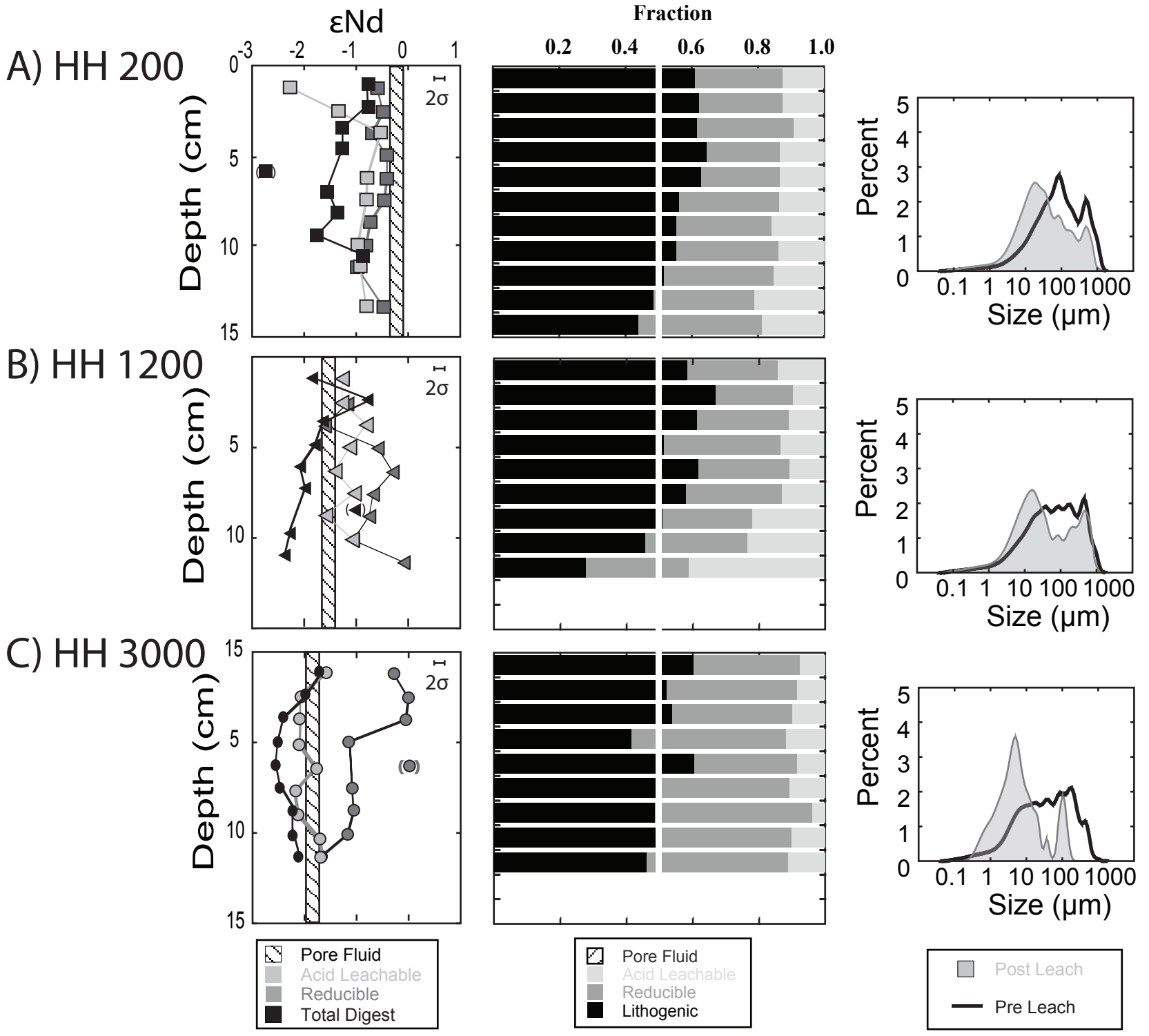
A) HH 200
B) HH 1200
C) HH 3000
εNd
Fraction
Depth (cm)
2σ
Percent
Size (μm)
0.1 1 10 100 1000
Pore Fluid
Acid Leachable
Reducible
Total Digest
Lithogenic
Post Leach
Pre Leach

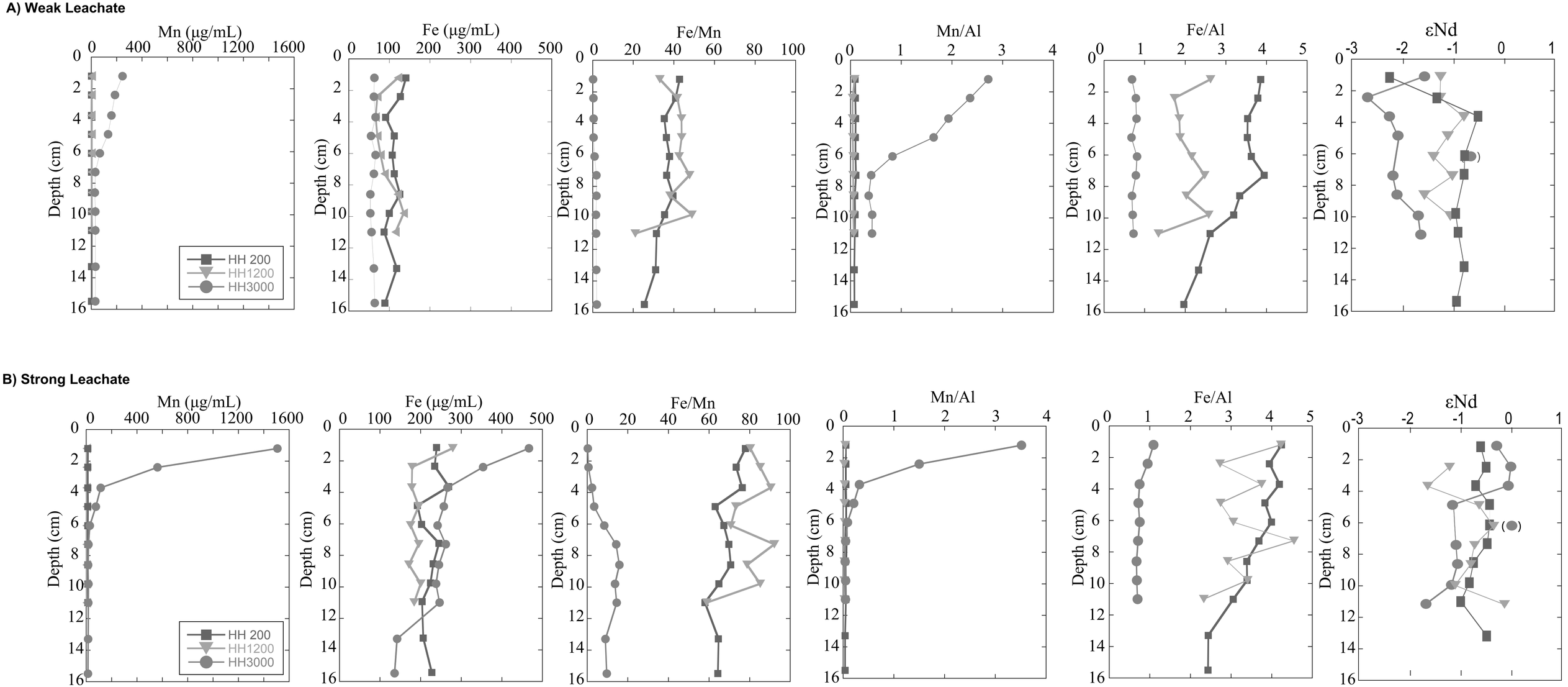
A) Weak Leachate
Mn (µg/mL)
Fe (µg/mL)
Fe/Mn
Mn/Al
Fe/Al
εNd
Depth (cm)
HH 200
HH1200
HH3000
B) Strong Leachate
Mn (µg/mL)
Fe (µg/mL)
Fe/Mn
Mn/Al
Fe/Al
εNd
Depth (cm)
HH 200
HH1200
HH3000

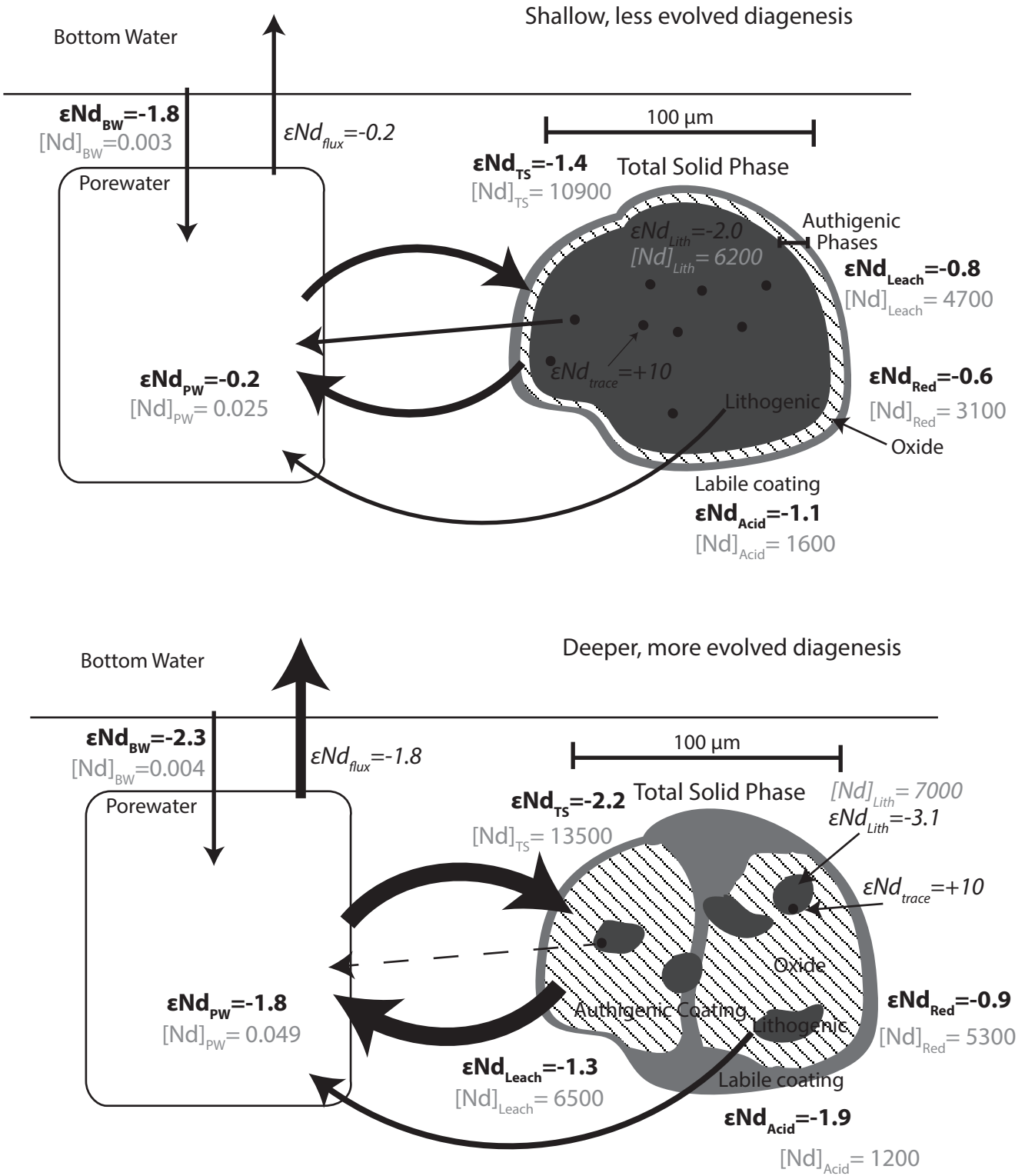
Shallow, less evolved diagenesis
Bottom Water
εNd_BW=-1.8
[Nd]_BW=0.003
εNd_flux=-0.2
Porewater
100 µm
εNd_TS=-1.4
[Nd]_TS= 10900
Total Solid Phase
εNd_Lith=-2.0
[Nd]_Lith= 6200
Authigenic Phases
εNd_Leach=-0.8
[Nd]_Leach= 4700
εNd_trace=+10
εNd_PW=-0.2
[Nd]_PW= 0.025
εNd_Red=-0.6
[Nd]_Red= 3100
Lithogenic
Oxide
Labile coating
εNd_Acid=-1.1
[Nd]_Acid= 1600
Deeper, more evolved diagenesis
Bottom Water
εNd_BW=-2.3
[Nd]_BW=0.004
εNd_flux=-1.8
Porewater
100 µm
εNd_TS=-2.2
[Nd]_TS= 13500
Total Solid Phase
[Nd]_Lith= 7000
εNd_Lith=-3.1
εNd_trace=+10
Oxide
εNd_PW=-1.8
[Nd]_PW= 0.049
Authigenic Coating
Lithogenic
εNd_Red=-0.9
[Nd]_Red= 5300
εNd_Leach=-1.3
[Nd]_Leach= 6500
Labile coating
εNd_Acid=-1.9
[Nd]_Acid= 1200

Table 1 *Reservoir ε_{Nd}.* Site average ε_{Nd} and Nd concentrations for bottom water, pore fluid, total leachate, acid leachable fraction, reducible leachate, total solid, and lithogenic reservoirs for HH200, HH1200, and HH3000. Concentrations are in ng cm^{-3}. The total leachate is a weighted average of the acid leachable and reducible leachates. The total solid includes the lithogenic and total leachate reservoirs. * indicates unfiltered bottom water. Reservoirs for which ε_{Nd} was calculated instead of measured directly are indicated by **. [a] the average pore fluid ε_{Nd} for HH1200 excludes the upper two intervals. Including the intervals the average pore fluid ε_{Nd} for HH1200 would be -1.9.

	HH200		HH1200		HH3000	
	εNd	[Nd]	εNd	[Nd]	εNd	[Nd]
Bottom Water	-1.8; 0.7*	0.003; 0.004*	-2.5	0.004	-2.3	0.004
Pore Fluid	-0.2	0.025	-1.5[a]	0.035	-1.8	0.049
Total Leachate**	-0.8	4700	-1.0	5700	-1.3	6500
Acid Leachable	-1.1	1600	-1.2	2200	-1.9	1200
Reducable	-0.6	3100	-0.8	3500	-0.9	5300
Total Solid	-1.4	16000	-1.5	18000	-2.2	20000
Lithogenic**	-2.0	6200	-2.5	6500	-3.2	7000

Table 1

Supplemental Information

Additional Methods

Sediment sampling

Cores were collected using a multi-corer (Barnett et al., 1994) and sectioned in an anoxic (N_2) glove bag into intervals. The intervals were operationally defined as the amount of sediment required to fill an 85 mL centrifuge vial. On average, these intervals represent 1.2 cm of depth in the core. After sectioning, the samples were centrifuged at between 10,000 and 12,000 rpm for 15 minutes. Pore fluid was then filtered using acid-clean syringes and PALL ® acrodisc syringe filters with a 0.45µm Supor ® membrane. Pore fluids from equivalent depth intervals from multiple cores were combined into large volume samples (250-750 ml) and acidified to pH ≤2.0 using trace metal clean ~11 M HCl while at sea. The sediment in the centrifuge tube was frozen after pore fluid removal, and remained frozen until they were freeze dried.

A single core was used for solid phase analysis at each site. The solid phase analyses included total sediment digestion (total solid), Carbon-Nitrogen-Sulfur (CNS) analysis, x-ray diffraction (XRD), grain size, and chemical leaching as described below. We measured total carbon on a PerkinElmer Series 11 CNHSO Analyzer and inorganic carbon on a UCI Inc. Coulometrics CMS130 Coulometer. NRC Beaufort Sea marine sediment reference material MESS3 was analyzed resulting in % total inorganic carbon (TIC) 0.66 ± 0.04, %total carbon (TC) 2.09 ±0.08, %total nitrogen (TN) 0.17 ±0.03, and %total sulfur (TS) 0.10 ±0.04. Organic carbon is calculated as the difference between total carbon and inorganic carbon. Sediment

grain size distributions for HH200, HH1200, and HH3000 were measured on a Beckman Coulter LS 13 320 multi-wavelength Laser Diffraction Particle size Analyzer and analyzed for major mineralogy by XRD at Oregon State University. Beckman Coulter® LS Control G15 and Latron 300 LS were analyzed at the beginning of each run and validated against Beckman Coulter® precision guidelines. An in-house bimodal control (250 and 550 μm) was also analyzed during each run. Bulk sediment samples were loaded with dispersant and sonicated before analysis. Leached sediment samples were also loaded with dispersant but were not sonicated prior to analysis. Measurements are reported in 116 size bins between 0.4 and 1822 μm for each sample (**Supplemental Information Table 1**). Sediments from all sites were digested in a mixture of HNO_3, HCl and HF using a CEM Corp MARS-5 microwave following the procedures of Muratli et al. (2012). For HH200, these sediments came from a separate sectioned core. For HH1200 and HH3000 these sediments came from the centrifuge tubes following pore fluid extraction.

Reservoir Comparisons

The direct comparison of Nd in each reservoir required concentrations in each reservoir to be normalized by volume. For this calculation, we assumed a porosity of 70% and a sediment density of 2.6 g cm^{-2}. Specifically, pore fluid Nd per cubic centimeter ($[Nd]_{vPW}$) was calculated as:

$$[Nd]_{vPW} = \frac{pM}{1000} \times P \times \frac{M}{1000} \quad \text{(Eq. 1)}$$

wherein pM is the measured picomolar concentration of Nd in pore fluids, P is the porosity, and M is the atomic mass of Nd in grams mol^{-1}. Weak and strong leachate Nd per cubic centimeter ($[Nd]_{vL}$) were calculated as:

$$[Nd]_{vL} = [Nd]_{L} \times (1 - P) \times \rho \quad \text{(Eq. 2)}$$

wherein $[Nd]_{L}$ is the measured ng Nd g^{-1} dry leached sediment, P is the porosity, and ρ is the sediment density. The lithogenic Nd per cubic centimeter ($[Nd]_{vLith}$) was calculated as:

$$[Nd]_{vLith} = [[Nd]_{Lith} \times (1 - P) \times \rho] - \Sigma[Nd]_{vL} \quad \text{(Eq. 3)}$$

wherein $[Nd]_{Lith}$ is the calculated ng Nd g^{-1} sediment remaining after the leach procedures, P is the porosity, ρ is the sediment density, and $\Sigma[Nd]_{vL}$ is the sum of the weak and strong leachate Nd per cubic centimeter. Even with the assumption that pore fluid occupies 70% of the volume of any given cubic centimeter, the Nd in the pore fluid reservoir remains <0.001% of the total Nd in that area for all sites (**supplemental information table 7**).

Supplemental Table Captions

SI Table 1 *Grain Size Distributions.* **A)** Summary of grain size data including the range and average peak grain size for the largest two peaks in each bimodal distribution for pre-leach and post-leach samples and the difference between the pre-leach and post-leach peak grain size. **B)** Grain size data for each bin for all samples from HH200, HH1200, and HH3000. Replicates are included where available. The average distribution for pre-leach and post-leach distributions are provided by site.

SI Table 2 *Pore Fluid Characteristics.* Dissolved Fe, Mn, Si and P from centrifuged pore fluids from HH200, HH1200, and HH3000. Dissolved Li, B, Sr, Ba, S, Si, and P from pore fluids collected by rhizon for HH1200 and HH3000.

SI Table 3 *Total Solid.* Neodymium and strontium isotope compositions, REEs concentrations, and accessory data for total solid from HH200, HH1200, and HH3000. The minimum detection limit (MDL) is provided in the case of a measurement below minimum detection limit (BMDL).

SI Table 4 *Leachate Accessory Elements.* Accessory data for leachate samples. All accessory elements measured on second leaching experiment unless otherwise noted by a * next to top depth. The minimum detection limit (MDL) is provided in the case of a measurement below minimum detection limit (BMDL).

SI Table 5 *Leachate Isotopes.* Neodymium isotopic composition and strontium isotopic composition of both acid leachable and reducible leachates for HH200, HH1200, and HH3000. The depths provided are the top of the interval in the sediment core.

SI Table 6 *Leachate REEs.* Concentration of REEs in each leachate normalized to pre-leach dry sediment weight (ng REE/g sed). Leach type and sediment depth provided for each sample. Number after leach type indicates leach experiment. Not all samples were leached during both experiments, all results are provided.

SI Table 7 *Reservoir Comparison.* Amount (in ng) of Nd in the acid leachable fraction, reducible fraction, pore fluid, and remaining lithogenic reservoirs normalized to a volume of one cubic centimeter. For these calculations, we assume a porosity of 70% and a sediment density of 2.6 g cm^{-2}.

Supplemental Figure Captions

SI Figure 1 *XRD Mineralogy.* **a)** Comparison of pre-leach (yellow) and post-leach mineralogy. The only significant difference is the loss of halite (red circle). **b)** Comparison of post-leach mineralogy from HH200, HH1200, and HH3000. All samples consist of quartz, albite, a white mica (e.g. illite or muscovite) and a chlorite mineral (e.g. clinochlore).

SI Figure 2 *Leachate Nd concentrations and* ε_{Nd}. Nd concentration and ε_{Nd} profiles for both reducible (black) and acid leachable (blue) fractions at HH200 (squares), HH1200 (triangles), and HH3000 (circles). Concentration profiles are shown for repeated leaching experiments (acid leachable (1) and (2) and reducible (1) and (2) while isotope profiles represent a composite from both experiments. Only the bottom two intervals were re-leached from HH3000.

Additional References

Barnett, P.R.O., Watson, J., and Connely, D. (1984). A multiple corer for taking virtually undisturbed samples from shelf, bathyal, and abyssal sediments. *Oceanologica Acta,* **7**, 399-408.

Muratli, J.M., McManus, J., Mix, A., and Chase, Z. (2012). Dissolution of fluoride complexes following microwave-assisted hydrofluoric acid digestion of marine sediments. *Talanta*, **89**, 195-200. doi: 10.1016/j.talanta.2011.11.081

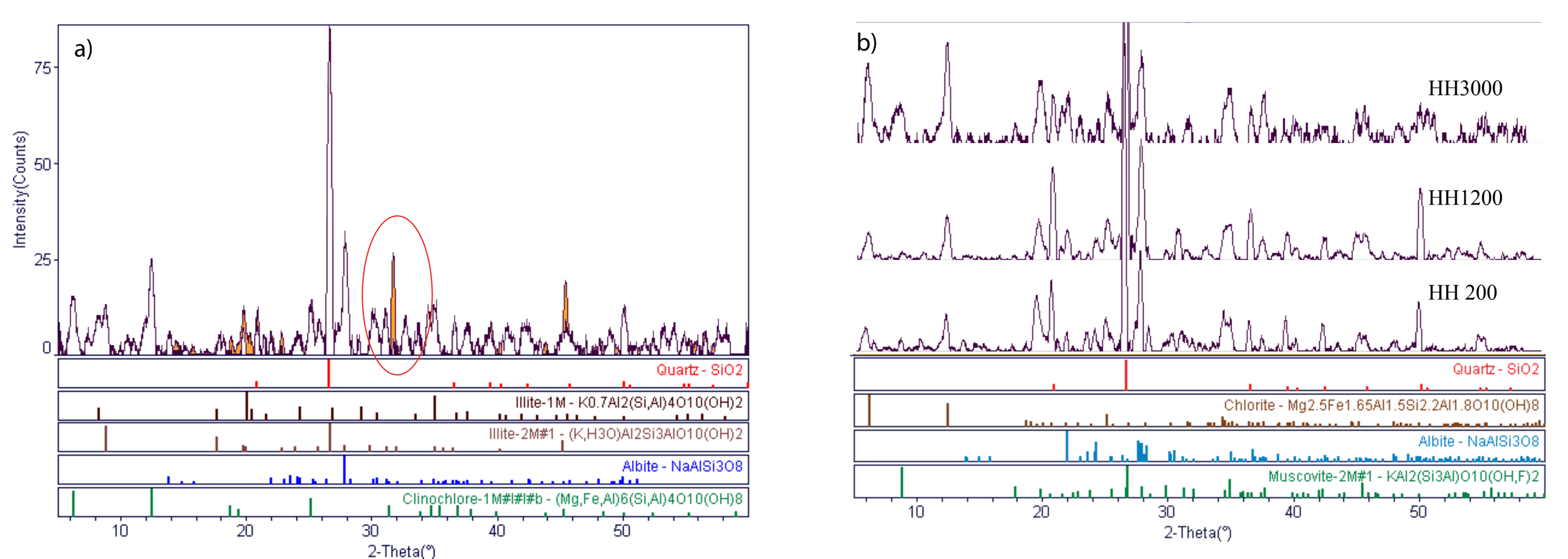
a)
Intensity(Counts)
75
50
25
0
Quartz - SiO2
Illite-1M - K0.7Al2(Si,Al)4O10(OH)2
Illite-2M#1 - (K,H3O)Al2Si3AlO10(OH)2
Albite - NaAlSi3O8
Clinochlore-1M#I#I#b - (Mg,Fe,Al)6(Si,Al)4O10(OH)8
10
20
30
40
50
2-Theta(°)
b)
HH3000
HH1200
HH 200
Quartz - SiO2
Chlorite - Mg2.5Fe1.65Al1.5Si2.2Al1.8O10(OH)8
Albite - NaAlSi3O8
Muscovite-2M#1 - KAl2(Si3Al)O10(OH,F)2
10
20
30
40
50
2-Theta(°)

SI Figure 2

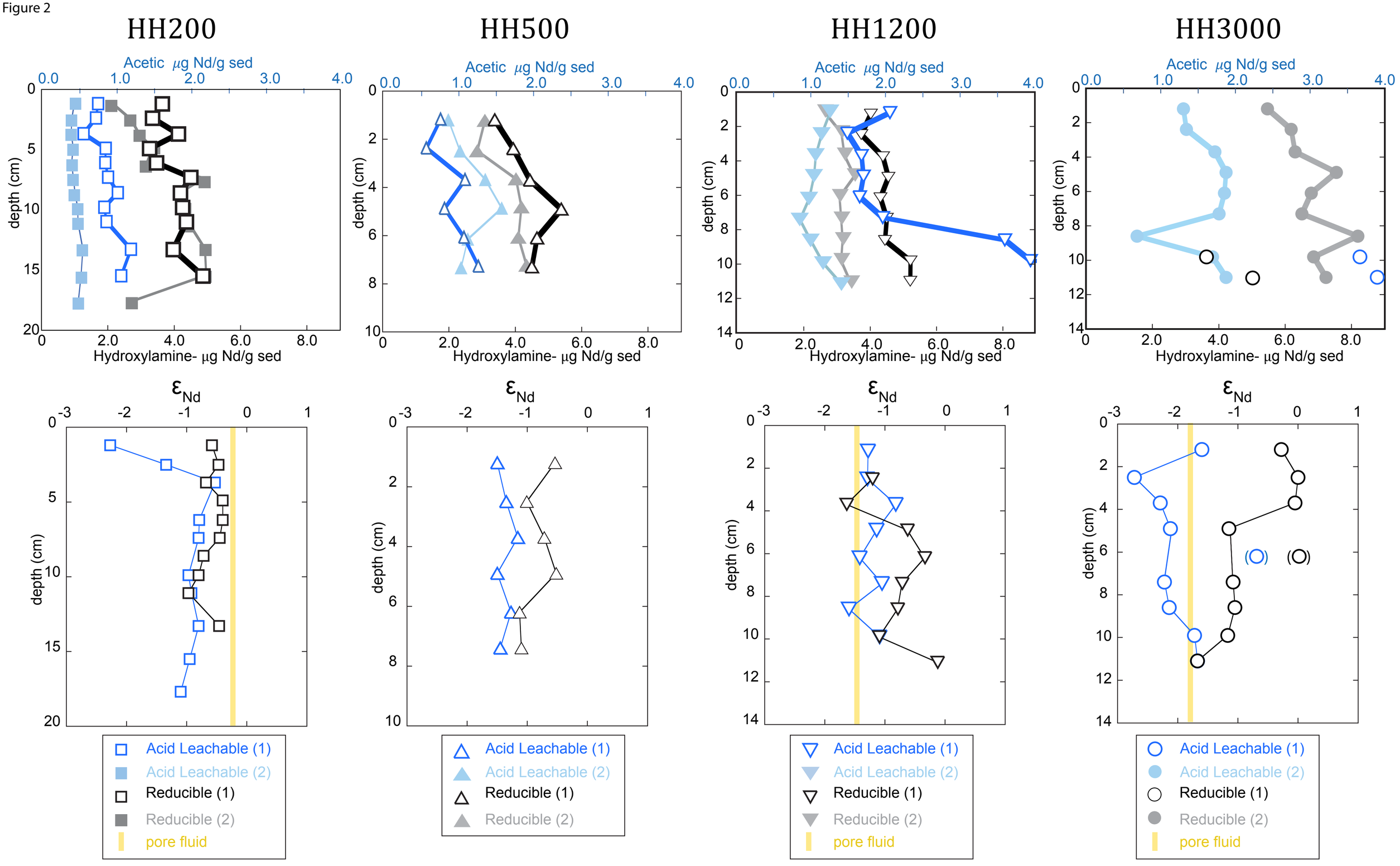
HH200
HH500
HH1200
HH3000
Acetic μg Nd/g sed
Hydroxylamine- μg Nd/g sed
depth (cm)
εNd
Acid Leachable (1)
Acid Leachable (2)
Reducible (1)
Reducible (2)
pore fluid